„This is the peer reviewed version of the following article: Bin Cai, Sebastian Henning, Juan Herranz, Thomas J. Schmidt and Alexander Eychmüller (2017). Nanostructuring noble metals as unsupported electrocatalysts for polymer electrolyte fuel cells. Advanced Energy Materials, 2017, Volume 7, Issue 23, pp.1700548, which has been published in final form at DOI:10.1002/aenm.201700548.

Nanostructuring noble metals as unsupported electrocatalysts for polymer electrolyte fuel cells

Bin Cai†, Sebastian Henning†, Juan Herranz, Thomas J. Schmidt and Alexander Eychmüller**

Bin Cai†, Prof. Dr. Alexander Eychmüller
Physical Chemistry, Technische Universität Dresden
Bergstraße 66b, 01062 Dresden, Germany
E-mail: alexander.eychmueller@chemie.tu-dresden.de
Sebastian Henning†, Dr. Juan Herranz, Prof. Dr. Thomas J. Schmidt
Electrochemistry Laboratory, Paul Scherrer Institut,
5232 Villigen, Switzerland
Prof. Dr. Thomas J. Schmidt
Laboratory of Physical Chemistry, ETH Zurich,
8093 Zurich, Switzerland
† These authors contributed equally to this work.

Keywords: unsupported electrocatalyst, metallic aerogel, oxygen reduction reaction, fuel cell, nanomaterial

Two major challenges that impede fuel cell technology breakthrough are the insufficient activity of the electrocatalysts for the oxygen reduction reaction and their degradation during operation, caused by the potential-induced corrosion of their carbon-support upon fuel cell operation. Unsupported electrocatalysts derived from tailored noble-metal nanostructures are superior to the conventional carbon-supported Pt nanoparticle catalysts and address these barriers by fine-tuning the surface composition and eliminating the support. Herein, recent efforts and achievements in the design, synthesis and characterization of unsupported electrocatalysts are reviewed, paying special attention to noble-metal aerogels, nano/meso-structured thin films and template-derived

metal nanoarchitectures. Their electrocatalytic performances for oxygen reduction are compared and discussed, and examples of successful catalyst transfer to polymer electrolyte fuel cells are highlighted. This report aims to demonstrate the potential and challenges of implementing unsupported catalysts in fuel cells, thereby providing a perspective on the further development of these materials.

1. Introduction

Ever-increasing, energy-related environmental pollution has prompted scientific and industrial research for clean and sustainable energy sources and conversion devices to ultimately replace current fossil-fuel-based energy systems.[1] Fuel cells operated with hydrogen and oxygen (air) are widely believed to be among the next generation of energy conversion systems owing to their high efficiency and low emissions.[2, 3] Polymer electrolyte fuel cells (PEFCs) feature low operating temperature, high power density, and high energy conversion efficiency, making it one of the most promising technologies for automotive or stationary applications.[4, 5] One of the major obstacles for the broad application of PEFCs is the lack of low-cost, durable and efficient electrocatalysts for the cathodic oxygen reduction reaction (ORR), whereby the slow kinetics of this reaction lead to major voltage losses in the fuel cells.[6-10] Numerous nanostructured materials have been developed in the past decades for catalyzing the ORR, including Pt-based metallic structures [11-13] and heteroatom-doped carbon materials.[14-16] Among them, former remains the top choice for industrial development due to their high performance, even if Pt is a scarce and expensive metal.[7] Therefore, reducing the Pt loading while maintaining or even improving the catalytic performance is an important cost reduction lever.

Recent research efforts in this direction have led to significant improvements of Pt-based electrocatalysts in terms of morphology engineering (nanostructured polyhedrons, wires, rods,

tubes, core-shell structures, etc.), composition manipulation (alloying with Pd, Au, Ni, Co, Cu, etc.), size control (down to 2-5 nm) and composite developments (support on carbon nanotubes, graphene, etc.).[17, 18] In most cases, these as-synthesized electrocatalysts are supported on carbon black and rely on its high surface area to obtain adequate active site dispersion. However, the carbon support is partially responsible for the insufficient catalyst durability, since it corrodes under the high potential conditions (up to 1.6 V) that are present during PEFC start-up/shut-down and local fuel starvation, leading to catalyst particle detachment and loss of electrical contact.[19, 20] While carbon corrosion rates can be reduced by switching to graphitized carbons with lower surface area, support stability remains an important concern.[21, 22] Unsupported electrocatalysts such as pure metallic aerogels, nano/meso-structured films, nanowires and porous nanostructures, provide opportunities to overcome this issue and are potentially less susceptible to other degradation phenomena observed under normal PEFC operation, such as catalyst particle migration, dissolution and Ostwald ripening, due to their extended surface areas.[20, 23] Ultimately, these electrocatalysts have to be processed into electrically conductive PEFC catalyst layers that must also provide mass transfer pathways for oxygen/air.[24] Their self-supportability leads to a direct contact of the electroactive species with the conductive substrates, thus assuring a good integrity of the catalyst layers. Besides, these unsupported electrocatalysts also feature large surface area, high porosity mechanical stability and extended metallic backbones, which are beneficial for successful implementations.[19]

To realize the elimination of the carbon support, different types of unsupported metallic nanostructures have been developed and tested as electrocatalysts for the ORR in PEFCs. These include: i) noble metal based aerogels with controlled compositions and morphologies that are synthesized by gelation of metal colloidal nanoparticles (NPs), e.g. alloyed Pd_xPt_y aerogels,[25]

Pt_xNi_y aerogels,[26] Pt_xCu_y aerogels,[27] etc.; ii) multi/bimetallic nano/meso-structured thin film catalysts with extended surface, tunable composition and controlled morphology that are prepared by physical vapor deposition;[28-31] iii) template-derived Pt-based nanostructures with controlled morphologies, such as core-shell structures with Pt surfaces (using Pd,[32] Cu,[33] Co[34] nanowires as the template), intermetallic FePt nanotubes (with electrospun Si nanofibers as the template),[35] PtFe hollow nanocapsule structure (silica particles as the template),[36] etc.

Considering the afore-mentioned aspects, this report summarizes the recent progress in the design and synthesis of unsupported metallic nanostructures. Their physical and chemical properties, i.e. morphology, surface area, porosity and electrochemical behavior, are correlated to the synthesis method and discussed further. Notably, the wide-spread use of measurements in liquid half cells to assess the materials' ORR activity allows for a comprehensive comparison among them, whereas due to the small amount of available data, the review of PEFC tests only covers selected examples. A better understanding of synthesis, resulting nanostructures and subsequent catalytic performance in the technical system is expected to pave the way to performance-oriented design and engineering of unsupported electrocatalysts. Finally, a perspective on future challenges and possible trends in unsupported electrocatalysts for PEFCs implementation is given.

2. Synthesis and Characterizations of Unsupported Electrocatalysts

2.1. Noble-metal Based Aerogels

2.1.1 Synthesis and features

Metallic aerogels, assembled from noble metal colloidal NPs, are of enormous scientific and technological interest owing to their ultralow density, high surface area, and large open interconnected pores.[37] The metallic aerogels combine the noble metal properties (e.g. catalytic activity, electric conductivity) with large surface area (providing more reactive sites), high porosity (facilitating mass transfer), and self-supportability (eliminating the need for a carbon support), thus rendering these noble metal aerogels promising candidates for electrocatalysis.[37] As a proof-of-concept, metallic aerogels with compositions of pure Pd and Au, as well as alloyed Pd_xPt_y, Pt_xNi_y and Pt_xCu_y have been synthesized and evaluated for electrocatalysis, as it will be further discussed in section 3.[25, 26, 38-40] Linking aerogel research and nanotechnology, hierarchical aerogels with primary and secondary pore structures, built from shape-engineered NPs, have also been reported in the form of either hollow shell or dendritic particles.[41-43]

As illustrated in **Figure 1**, the general synthesis of noble metal aerogels via the sol-gel process consists of three steps: i) the synthesis of nano-sized building blocks (NBBs); ii) the gelation of the NBBs into hydrogels (plus shape-control of the hydrogel) and iii) the supercritical drying of the hydrogel to yield an aerogel. These three strategies are outlined in different colors in paths I (B1-H1-A1), II (B1-H1-H2-A2) and III (B1-B2-H3-A3) of **Figure 1**. In strategy I, solid noble metal NPs with controlled compositions are employed as NBBs, thus resulting in a nanowire-based aerogel. Citrate and cyclodextrin are frequently utilized as the stabilizers to narrow the size distribution of the metal NPs.[44] The relatively weak coordination interaction between the stabilizer and metal NPs is critical for the gelation step (from B1 to H1 in **Figure 1**), which can be realized *via* an spontaneous gelation process[25, 26, 38] or via controlled destabilizations (by heating[45] or adding salt[46] and cross-linkers[47]).

Besides the porous and interconnected 3D network structure, hierarchical aerogels also possess backbones with locally modified morphologies instead of solid nanochains. As shown in **Figure** 1, this sub-structure can be obtained either by tailoring the hydrogel *via* strategy II (B1-H1-H2-A2)[43] or engineering the NBBs *via* strategy III (B1-B2-H3-A3).[41] At present, research on metallic hierarchical aerogels prepared by manipulation of the NBBs is still in its infancy and lags far behind the abundance of colloidal metallic nanoarchitectures.[48] This may be ascribed to the frequent requirement of strong stabilizers for the shape-control of the metallic NPs, which is extremely detrimental to the subsequent gelation/destabilization of these colloids.[44] Future research may focus on realizing the gelation by controlled chemical/physical removal/complexation of the surface ligands, or by adjusting the chemical parameters of the solvent (e.g. ionic strength, dielectric coefficient).

2.1.2 Wire-based aerogels

The synthesis of metallic aerogels following strategy I (**Figure 1**) generally yields wire-based aerogels. The nanowire-like backbones are derived from the fusion and connection of the particulate NBBs (mostly noble metal NPs) during the gelation process. Depending on the elemental composition and distribution, these aerogels can be divided into three types: monometallic aerogels (Pd, Pt, Au, Ag),[38, 39, 46, 47] bimetallic alloy aerogels (Pd_xPt_y, Pt_xNi, Pt_xCu, etc),[25, 26, 49] and mixed multi/bi-metallic aerogels (Au-Pd, Pd-Pt, Au-Ag-Pt, *etc*.).[45, 50] **Figure 2** shows the representative scanning electron microscopy (SEM) and transmission electron microscopy (TEM) images of the wire-based aerogels. They all exhibit high porosity with numerous open pores and similar 3D network structures with extended nanowires interconnected randomly. The nanowire-like backbones show similar diameters to those of the original NPs,

confirming the presumption that the hydrogel formed from the starting NPs without any intermediate agglomeration steps.

Using citrate-stabilized Pd NPs as the NBBs, pure Pd aerogels were obtained by destabilizing the concentrated colloidal sols by either heat treatment[45] or adding calcium ions[47]. Following a similar strategy, Ag and Pt aerogels were fabricated using H_2O_2 and ethanol as the destabilizer.[46] It should be pointed out that the concentration step of as-prepared NPs required for these approaches, however, is usually time-consuming, thereby limiting scale-up of the synthesis. To address this, spontaneous gelation of the *in situ* generated NPs with[38] or without[25] the modification of cyclodextrins was developed to synthesize Pd (**Figure 2a-c**) and Pt aerogels. In a similar way, Au aerogels (**Figure 2d-f**) were synthesized by a dopamine-induced gelation of the as-prepared Au NPs based on the complexation between dopamine and Au.[39] To endow aerogels with additional properties, bimetallic Pd_xPt_y aerogels with tunable composition were prepared based on the spontaneous gelation method (**Figure 2g-i**).[25] Following the same strategy, Pt-based aerogels with compositions of Pt_3Ni (**Figure 2j-l**), $Pt_{1.5}Ni$, Pt_3Cu and PtCu were also fabricated and investigated as ORR electrocatalysts.[26, 27] To accelerate hydrogel formation, Zhu *et al.* reported a series of MCu (with M = Pd, Pt, or Au) bimetallic aerogels based on the in situ reduction of metal precursors at elevated temperature, thereby indeed observing an enhancement of the gelation kinetics.[49]

The average density of the metallic aerogels was estimated to be 0.016 – 0.050 g cm^{-3}, which amounts to approximately one thousandth of that of the corresponding bulk materials. Their porosity and surface area were further investigated by N_2 physisorption measurements. The N_2 adsorption-desorption isotherms obtained from all these metallic aerogels show a combination of the characteristics of type II and type IV isotherms (**Figure 3a-c**), indicating the wide-spread

presence of both meso- and macro-pores within the aerogel structures. The specific surface areas of the aerogels determined based on the Brunauer−Emmett−Teller (BET) method are in the range of 32 - 168 $m^2 g^{-1}$. As shown in **Figure 3d-e**, the metallic aerogels revealed a wide pore size distribution in the aerogels ranging from micropores to meso/macropores, which could also be observed in the SEM and TEM images (**Figure 2 and 4**). The hierarchical pore systems hold the potential for reducing the diffusion barriers in catalysis applications since the diffusion rates through 10−50 nm pores can approach those of molecules in open media.[51]

2.1.3 Hierarchical aerogels

Following strategies II and III in **Figure 1**, hierarchical aerogels that generally combine a 3D interconnected porous structure on the macroscale and a fine-tuned configuration of local backbones at the nanoscale can be obtained (**Figure 4**). This combination usually leads to an integration of several catalysis enhancement factors in hierarchical aerogels. Recently, PdNi hollow nanospheres (HNSs) were employed as NBBs to fabricate a hierarchical aerogel with a well-defined 3D necklace-like network structure (**Figure 4a-c**).[41] The hollow cavity distributed throughout the networks could further be identified by a distinct peak (at ca. 22 nm) in the pore size distribution analysis (**Figure 3f**). This aerogel exhibited an improved electrocatalytic activity for ethanol oxidation when compared to the isolated HNSs and Pd/C. Subsequently, a series of hierarchical aerogels were synthesized from the gelation of colloidal Ni-Pd_xPt_y NBBs with continuously engineered shape and varied composition.[42] Taking the extreme composition of Ni-Pt as an example (**Figure 4d-f**), low magnification SEM/TEM images reveal that this hierarchical aerogel features a porous structure similar to that of the wire-based aerogel while exhibiting a dendritic morphology at the nanoscale. In addition, Arachchige *et al*. reported a salt-

mediated method to self-assemble AuAg, PdAg and PtAg nanoshells into a gel structure.[52] Thiolate-coated Ag nanoshells with varying size and shell thickness were then assembled into monolithic hydro/aerogels via oxidative removal of the surface thiolates.[53]

By taking advantage of hydrogel engineering, PtAg nanotubular aerogels were fabricated via a simple galvanic replacement reaction between the in situ, spontaneously gelated Ag hydrogel and the Pt precursor.[43] As shown in **Figure 4g-i**, the resulting PtAg aerogels possess hierarchical porous network features with primary macro-pores from the aerogel network and secondary micro-pores from the porous surface of the nanotube-backbones, resulting in high porosities and large specific surface areas. Due to its unique structure, the as-prepared PtAg aerogel exhibits 19-fold enhanced electrocatalytic activity towards formic acid oxidation as compared to Pt black.[43]

2.2 Nano/meso-structured Thin Films

Another unique category of unsupported electrocatalysts are Pt-based meso- and nano-structured thin films (MSTFs and NSTFs), developed by 3M using magnetron sputter deposition of Pt thin film alloys on crystalline organic whiskers.[28, 54, 55] **Figure 5a** illustrates the step-by-step preparation process of the NSTFs as well as their transformation to MSTFs via annealing in a reductive atmosphere. The support is a thin layer of an oriented array of crystalline organic whiskers, namely perylene red, with diameters of less than 1 μm tall and 30 nm × 55 nm in cross-section and a number density of ≈35 whiskers μm^{-2}.[30] These non-conductive and electrochemically stable organic whiskers eliminate carbon corrosion, and their crystallinity facilitates the subsequent nucleation and thin film growth of the sputtered catalyst materials. To date, a series of Pt-based NSTF catalysts (Pt-Ni, Pt-Co, Pt-Ir, Pt-Co-Ni, Pt-Co-Mn, Pt-Co-Fe,

etc.) with well-defined extended and nanoscale surfaces have been developed by sputtering the catalyst layer onto the whisker substrate.[7, 28, 30, 54, 56] Their unique thin film structure significantly reduces the population of low-coordination number atoms and hence increases the surface specific activity for ORR about 5-10 times with respect to commercial Pt/C catalysts, which is in line with the activity values of polycrystalline or single crystal bulk surfaces.[30] Since the NSTF catalysts already exhibit large extended metal surfaces, they are less susceptible to the loss of surface area, thus enhancing their durability. In addition, the elimination of carbon corrosion at high voltage makes them particularly useful as PEFC anode where high tolerance to anode fuel starvation events and cell reversal are required.[54]

The highly corrugated surface of as-sputtered NSTFs occupied by pyramid-like pillars with a cross-section of ≈6 nm can be gradually smoothed by heating up to 400 ^{o}C in a reductive atmosphere.[29] As depicted in **Figure 5b-c**, the annealing process triggers the transformation from NSTFs to MSTFs while retaining the whisker's vertically aligned morphology, even if the organic whisker support is completely removed. In situ high resolution TEM (**Figure 5c-d**) illustrates that the initially corrugated surface morphology is transformed into a more homogeneous, flat and ordered thin film with large crystalline domains (20–40 nm). Simultaneously, the fraction of undercoordinated sites is further reduced, since (111) surface facets start to prevail, thereby promising improved activity for ORR. Indeed, as claimed by Stamenkovic et al., NSTF catalysts can successfully mimic the catalytic behavior of polycrystalline bulk materials, whereas Pt alloy MSTF catalysts exceed the activity of the latter.[29] For instance, PtNi MSTFs show a remarkable 20-fold enhancement in the ORR activity over commercial Pt/C, which will be discussed in the following sections. Thin film catalyst composed of vertically aligned Pt-Ni nanorod-arrays has also been fabricated by a glancing angle

deposition technique, which leads to more dense arrays.[57] These findings provide a proof-of-concept for designing highly active and durable electrocatalysts by tailoring the composition, morphology and mesoscale structure of the thin-film-based materials.

In another study, Kibsgaard et al. reported a new synthesis for surface-extended Pt MSTF catalysts via electrodeposition of Pt into a mesoporous silica film that serves as a template.[31] As outlined in **Figure 5f**, the silica film with a double gyroid (DG) morphology was prepared by calcination of the surfactant-silica mixture and then removed after electro-filling with Pt. The resulting Pt DG MSTF maintains the interlocked, twisted network structure after removal of the silica, displaying a high porosity with an average pore-to-pore distance of 6.7 nm, and an average pore diameter of 3−4 nm. Similar to the MSTFs discussed above, the continuous nature of the DG-structured MSTFs promises improved stability due to the mitigation of Ostwald ripening and Pt migration/agglomeration and the suppression of carbon corrosion. Following a similar procedure, a Pt_xNi alloy was fabricated into a highly ordered DG-shaped mesoporous thin film.[58] The resulting Pt_xNi MSTF catalysts maintained the DG meso-structure and good activity after intensive accelerated stability testing, which shows the promise of mesoscale structured Pt-based ORR catalysts.

2.3 Template-derived Pt-based Nanostructures with Controlled Morphology

In addition to the thin film approaches introduced above, other template methods have been applied to prepare nano-sized Pt-based architectures with porous, hollow or core-shell structures.[59, 60] When used as electrocatalysts, these Pt-based nanostructures with relatively large diameters (about 50 nm to 100 nm) and extended surfaces frequently eliminate the need for a carbon support and provide electronic conductivity and porosity by themselves. Well-

established examples are the one-dimensional (1D) nanowires and nanotubes developed by the groups of Yan and Pivovar (as shown in **Figure 6a-c**, taking Pt-Co nanowires as an example).[61] For instance, Pt and PtPd nanotubes were synthesized via galvanic replacement of Ag nanowire templates, exhibiting an outer diameter of 50 nm, a length of 5–20 μm and a thickness of 4–7 nm.[62] Because of their unique combination of dimensions at multiple length scales, these nanotubes can provide high surface area owing to their nano-sized wall thickness without the need for a carbon support, thus exhibiting an ORR mass activity twice higher than Pt black. Porosity was subsequently added on the wall of the Pt nanotubes, thereby increasing the Pt normalized surface area and mass activity for ORR.[63] By replacing subsurface Pt with Pd, Pd-Pt core-shell nanotubes with size similar to the Pt nanotubes discussed above, were also studied in an effort to improve the Pt utilization for ORR.[32] By optimizing the Pt coating, this core-shelled electrocatalyst exceeded the DOE mass activity target on a Pt-normalized basis. After that, Cu, Ni and Co nanowires have sequentially been explored as templates to prepare Pt-shell nanowire ORR electrocatalysts which incorporate activity enhancements due to their extended Pt surfaces and the transition-metal alloying effect.[33, 34, 64] Varying the amount of the Pt precursor during galvanic replacement step of their synthesis allowed for the investigation of a wide range of compositions. Although these Pt-coated Cu/Ni/Co nanowires showed improved ORR activity and durability, it should be pointed out that the Pt-on-Co nanowire catalysts could feature low mechanical stability, because the Co nanowire 'core' is immediately etched upon exposure to acid, leaving only a Co-containing free-standing 'Pt shell' (nanotube) as the active catalyst material.[34] Recently, a follow-up study by the same group has showed that the Pt-Ni nanowires reached the most promising ORR performance after annealing at 200 ºC, due to the balancing of the initial activity and durability.[65]

Another example of unsupported 1D electrocatalysts are the PtFe ordered intermetallic nanotubes that are fabricated by coaxial nozzle electrospinning with separate core and shell solutions.[35] The core silica content in the as-spun nanofibers is subsequently removed by calcination in air, resulting in a recrystallization of the shell Fe/Pt contents into an intermetallic phase with an ordered face-centered tetragonal (fct) structure. The resulting fct PtFe nanotubes show an average outer diameter of ≈120 nm and 'infinite' length. This combination of multiple length scales allows discarding of the carbon support, and the materials' anisotropic morphology is expected to improve mass transport and proton conductivity in the electrode.[35]

In another report, surface-modified silica particles were employed to assemble Pt-Fe NPs, followed by dissolution of the silica template.[36] The resulting PtFe catalyst with a network structure consisting of porous and hollow capsule from interconnected nanoparticles exhibits a shell thickness and pore size of ≈10 nm and an outer diameter of ≈400 nm (**Figure 6d-e**). This unsupported catalyst enabled the formation of a thin cathode with a thickness of 1 - 1.5 μm, nearly one-fifth that of a conventional electrode, implementing a carbon-supported catalyst (see section 4 for details). The elimination of the carbon support in the catalyst layer resulted in high durability during start–stop durability tests, which are known to drastically degrade conventional catalysts.

Finally, ordered macroporous Pt electrodes with inverse opal structures were also applied as cathode catalysts in PEFCs.[66] The Pt inverse opal electrode was fabricated directly on thiol-modified gas diffusion layers (GDLs) by electrodeposition of the infiltrated Pt precursor, followed by removal of the self-assembled polystyrene template. The resulting electrode duplicated the hexagonal close-packed structure from the polystyrene beads, resulting in a periodic inverse opal structure with interconnected macropores and a large surface area and

volume (**Figure 6f**). As demonstrated in a practical PEFC, the periodic Pt cathode maintains an inverse opal structure entirely within a membrane electrode assembly (MEA) and leads to a robust and integrated configuration of catalyst layers. Therefore, the periodic structured electrode minimizes the loss of catalyst materials and maintains an effective porosity, as well as an improved mass transfer and effective water management, owing to its morphological advantages.[66]

3. Electrochemical Behavior of Unsupported Electrocatalysts in Liquid Half-cells

Liquid half-cell experiments are an efficient screening tool to identify interesting catalysts and to investigate reactivity determining factors; however, they are insufficient to predict the performance in a technical environment, as it will be shown in the following section 4. Nonetheless, in this section we will report on the electrochemical behavior of selected systems from section 2, focusing on their electrochemical surface area (ECSA) and ORR activity.

The latter ORR activity is commonly expressed as the mass or surface area normalized current at 0.9 V_{RHE}, obtained from polarization curves on thin film electrodes in O_2-saturated electrolyte in a rotating disk electrode (RDE) configuration.[67] As various literature report suggest,[68-70] the obtained activity values are tightly interlinked to the quality of the thin films, measurement conditions (e.g. scan rate) and data treatment (e.g. with/without correction for mass transfer limitations), making it challenging to compare measurements performed in different laboratories. Considering this limitation, we predominantly report results that were extracted at 0.9 V vs. the reversible hydrogen electrode (RHE) from anodic sweeps at scan rate 20 mVs^{-1} and a rotation speed of 1600 rpm in O_2-saturated 0.1 M $HClO_4$ electrolyte at room temperature.[68, 71] Activity values reported at different potential, e.g. 0.95 V_{RHE}, were extrapolated to 0.9 V_{RHE} assuming a

Tafel slope of 60 mV dec^{-1};[72] results at different scan rates were adapted considering the relation between current and scan rates investigated in Ref [68].

To qualify as an interesting material in such liquid half-cell screening tests, novel catalysts should meet the U.S. Department of Energy (DOE) mass activity target of 0.44 A/mg_{Pt}, which, strictly speaking, applies to an iR-free voltage of 0.9 V_{RHE} in a PEFC at 80°C with 150 kPa_{abs} and fully humidified hydrogen and oxygen fluxes.[21] A higher mass activity (MA) can either be achieved by boosting the turnover frequency of the active sites (typically expressed as the surface area normalized activity (SA) in mA/cm^{-2}_{Pt}) and/or by increasing the catalyst's dispersion (ECSA in m^2/g_{Pt}). The former goal is generally addressed by moving to Pt-alloy systems with a decreased surface binding energy of oxygenated species and an increased oxygen reduction rate .[73, 74]

The electrochemical behavior of the materials presented in section 2 that have been tested for ORR activity in RDE configuration are summarized in **Figure 7**; when multiple alloy compositions were investigated in the same reference, only the most active catalyst was included for greater clarity. Additionally, state-of-the-art carbon-supported catalysts, Pt/C (≈ 50 wt% Pt, Tanaka Kikinzoku KogyoK. K., TEC1050E)[70, 71] and dealloyed $PtNi_3/C$[75, 76] that are available via scalable synthesis routes were considered as benchmarks.

Interestingly, almost 50 % of the catalysts in **Figure 7** meet or exceed the DOE ORR mass activity target, proving that unsupported structures can go together with high catalytic performance and compete with state-of-the-art Pt alloy/C catalysts. Considering the difficulties when comparing data from different labs, **Figure 7b** displays the MA as an improvement factor vs. the Pt/C benchmark measured in the same study, which can help to further mitigate artifacts from unlike measuring conditions that cannot be accounted in our estimate (e.g., cleanliness of

the electrochemical measurement). Assuming a MA of ≈ 0.3 A/mg_{Pt} for Pt/C (averaged from the results reported in Refs.[70, 71]), an improvement factor of ≈ 1.5 as indicated by the red dotted line can be considered equal to reaching the 0.44 A/mg_{Pt} defined by the DOE. Applying this new criterion, additional samples meet the activity target.

Focusing on the promising materials in **Figure 7a-b**, it becomes obvious that preparing an alloy is critical to reach sufficient catalytic performance, as it is already well established for standard carbon supported materials.[7] Moreover, the synthesis of these active materials seems feasible by multiple pathways: wet chemical synthesis (Pt-Pd aerogel),[25] sputtering (NSTF,[28] MSTF[29]), galvanic replacement of a template (Pt-Ni nanowires),[64] melt spinning (nanoporous Pt_6Ni_1)[77] and template-assisted electrodeposition (double gyroid PtNi[58]). Upon comparison of **Figure 7c-d**, a reciprocal relation between SA and ECSA can be observed, whereby high ECSA values translate into low SA values. This trend, first studied for Pt/C catalysts with varying nanoparticle sizes, is referred to as particle-size-effect and explained by the enhanced adsorption of oxygen-containing spectator species at a given potential for smaller Pt particle sizes, thus reducing the surface-specific ORR activity.[10, 78] Moreover, **Figure 7d** reveals that some high-performance unsupported materials have very small ECSAs of ≈ 10 m^2/g_{Pt}, increasing the risk of surface contamination, electrode flooding and large local O_2-diffusion resistances in real PEFCs.[79] The following section that focuses on the FC performance of these promising materials will discuss the issues mentioned above and others in depth.

As part of electrochemical testing in liquid half-cells, catalyst materials are often subjected to an accelerated stress test to compare their durability to that of a Pt/C benchmark. Electrodes from numerous materials in **Figure 7** were cycled electrochemically up to 30000 times between ≈ 0.5 and ≈ 1.0 V_{RHE} at 50 mV s^{-1}, generally showing a less severe loss of ECSA than Pt/C and

maintaining end of life activities significantly greater than the benchmark.[25, 33, 34, 58, 64, 77, 80] Applying an accelerated stress test with a maximum potential limit of 1.5 V_{RHE}, similar to the DOE catalyst support testing protocol,[81] the stability advantages vs. Pt/C are likely to become even more dominant. The promising activity and durability in RDE experiments illustrates why many unsupported ORR catalysts should be tested in PEFCs to investigate their potential under real application conditions.

4. Transfer of the Unsupported Electrocatalysts to PEFCs

4.1. Function/Processes in the Catalyst layer

As described in the introduction, low temperature PEFCs consist of a MEA sandwiched between two bi-polar plates that provide an electrical pathway and access to the reactive gases (H_2 and O_2) through a gas channel network.[2] The MEA, sort of the heart of the fuel cell, is composed of anodic gas diffusion layer (GDL), anodic catalyst layer (CL), membrane, cathodic CL and cathode GDL. Each of these components has complementary roles and research to further improve them individually is necessary and ongoing. The outer GDLs transport reactants from the gas channels to the CLs, manage the water content in the cell and transfer electrons plus heat.[82, 83] The central membrane transports protons and water from anode to cathode, whilst acting as an electronic insulator to prevent cell short circuits. Lastly, the CLs convert the reactants electrochemically and control the circulation of electrons, protons, reactants and product water, thus playing a key role for overall fuel cell performance.[84] In order to better understand the requirements for the design of efficient catalysts layers, the processes mentioned above will be discussed in detail on the basis of a state-of-the-art Pt-M/C catalyst and exclusively regarding the cathodic CLs.[21, 85] This choice is motivated by the higher voltage losses at the

cathode vs. anode, caused by the extremely fast hydrogen oxidation reaction (HOR) kinetics on Pt and negligible gas diffusion resistances for H_2.[86] It goes without saying that the structure and thus performance of the CLs is profoundly influenced by the properties of the catalyst material itself.[87, 88] This renders CL design on an individual material basis necessary, yet provides opportunities to optimize the CL structure through targeted design of the catalyst materials.

To begin with, typical Pt-M/C CLs consist of the catalyst nanoparticles, carbon support, ionomer and pores,[21, 84, 87, 89] and can be described at three different scales, as illustrated in **Figure 8**.[87] At the microscale (< 10 nm), the electrochemical conversion of O_2 to H_2O takes place at the surface of Pt-M nanoparticles, whereby the number of active sites and reactivity is determined by shape, size and composition of the particles.[84, 90] In the absence of mass transport limitations, the reactivity of nanoparticles, expressed as a current density, can be described by the Butler-Volmer equation that relates current density and potential.[84, 91]

Looking at the mesoscale (tens of nm), the Pt-M nanoparticles are either located on the surface of carbon agglomerates (diameter of 50 – 300 nm)[87, 92] or inside of primary pores (2 – 20 nm)[87, 92] that are present in between the primary carbon particles (≈20 nm).[92] Naturally, for the electrochemical conversion to occur, Pt-M nanoparticles need access to electrons, O_2 and protons. Whereas the former is provided through the network of conductive carbon agglomerates that extends all the way to the GDL, oxygen and proton transport are more complex.

It has been experimentally observed that the ionomer forms a thin film around the carbon agglomerates,[93] the thickness being a function of the ionomer-to-carbon-ratio (I/C).[87] Nonetheless, there is proof that this thin film is not uniform in thickness and complete coverage is not achieved for all type of carbon supports, even at higher I/C-ratios.[87, 94] State-of-the-art perfluorosulfonic acid (PFSA) ionomers transport protons to the active sites through the sulfonic

acid groups attached to the polymer chain, whereby the conductivity is linked to acid strength, acid content (ion-exchange capacity IEC) and water content.[95] With primary pores being inaccessible to ionomer,[87, 95] proton transport to Pt-M nanoparticles inside the carbon agglomerates is only feasible if these pores are filled with water, making such conditions desirable to reach high performance.[21, 84]

To describe the transport process of O_2 gas to the active sites, the secondary pores between carbon agglomerates (≈ 20 – 100 nm [84], or up to 200 nm [96]) on the macroscale of the CL(cf. **Figure 8**) need to be considered. In optimized CLs under the desired PEFC operation conditions, these secondary pores, in contrast to the primary pores discussed earlier, ought to be free of liquid water to allow for effective gas transport from the GDL through molecular and Knudsen diffusion.[84, 97] Naturally, the transport effectiveness is also a function of the CL thickness, that depends on the loading (mg_{Pt}/cm^2_{MEA}), Pt concentration (wt % Pt/C) and I/C-ratio,[98] whereby the thicknesses usually amount to around 10 µm.[21, 84, 87, 89, 99] Ultimately, O_2 needs to pass, i.e. dissolve and diffuse, through the ionomer film to reach the active site. This step can be described as a local O_2 transport resistance that accounts for up to 50 % of the overpotential associated with O_2 transport losses in PEFC cathodes at low loadings (≈ 0.1 mg_{Pt}/cm^2_{MEA}) and high current densities > 1.5 A cm^{-2}_{MEA}.[79, 97] The resistance scales inversely with the Pt ECSA, i.e. great catalyst dispersion is advantageous, and the latest results indicate that the thin ionomer film's O_2 transport resistance is increased locally by the interaction with the Pt surface, thus pointing at advanced ionomer development as a key strategy to mitigate this issue.[79]

4.2. Advantages/Challenges of CLs with Supported vs. Unsupported Electrocatalysts

As mentioned in section 4.1., the structure of the CL is closely interlinked with the catalyst material used. This can for instance be illustrated by calculating the thickness of the CL when going from supported to unsupported catalysts. Considering a state-of-the-art 50 wt% Pt-M/C catalyst, at an I/C-ratio = 1, with a CL porosity of 60 %,[98, 100] a loading of 0.2 mg_{Pt}/cm^2_{MEA}, and assuming a ionomer and carbon densities of ≈ 2 g/cm^3,[10] the thickness amounts to ≈5 µm (thereby overlooking the negligible thickness contribution from Pt-M nanoparticles). Due to the 10-fold larger density of Pt vs. C, the removal of the carbon support upon transitioning to unsupported materials leads to an expected thickness of only ≈ 0.5 µm, ≈ 90 % lower than that of Pt/C CLs (assuming porosities of 60 % for both materials,[101] and an ionomer-to-catalyst ratio of 0.1 for the aerogel) and that can profoundly affect the optimal CL design.[84]

In principle, transitioning from supported to unsupported catalysts can entail alterations of electron, proton, reactant and product water transport. Envisioning unsupported catalysts either as extended Pt-M surfaces or Pt-M particulate NBBs (i.e. conductive materials), electron transport will occur similarly to Pt-M/C CLs. For the ultrathin CLs expected with unsupported catalysts as illustrated by the calculation above, it is reasonable to assume that the proton concentration is significantly increased and can approach the proton bulk concentration in the membrane.[84] Moreover, it has been found that purely metallic surfaces like the NSTFs from 3M,[102] which will be introduced in detail later, rely on proton conduction on the Pt surface and function well in the absence of ionomer.[79] While such proton conduction could be provided either by diffusion of H_2O or hydrogen adsorbed on the Pt-surface (H_{ad}), or by H^+-diffusion within very thin surface water films,[103] the latest results indicate the preponderating importance of the latter.[104, 105] As for reactant and product water transport, it is paramount for CLs derived from unsupported catalysts to exhibit appropriate porosities and pore size distributions to enable

diffusion between active sites and the GDL, as it is also the case for conventional CLs prepared with carbon supported catalysts (cf. section 4.1.). Keeping in mind that, in the latter case, this porosity is provided by the carbon support material exclusively, i.e. through the stacking of 50 - 300 nm large carbon agglomerates which results in free spaces,[92] retaining such property with unsupported catalysts and their potentially smaller agglomerate dimensions constitutes a major challenge for the preparation of the catalyst layer and should also be considered at the stage of catalyst synthesis. At the same time, the expected thinning of the CLs due to the use of unsupported catalysts will certainly alter mass transport properties and water distribution,[99] possibly translating into pore structure requirements different from the ones established for conventional CLs.

4.3. PEFC Tests of Unsupported Electrocatalysts

Considering the high complexity of the processes affecting the ORR performance in PEFCs vs. liquid half-cells, i.e. RDE experiments, it is not surprising that for many promising catalysts PEFC performance does not match RDE results.[5] This holds true for novel carbon-supported catalysts, like Pt_3Ni nanoframes,[106, 107] as well as for unsupported Pt-Ni nanowires for which preliminary experiments indicate similar discrepancies.[108] A part of this disagreement between PEFC and RDE can be explained considering the differences in measurement parameters such as temperature and potential control (often scanned vs. held in RDE vs. PEFC tests, respectively).[79] Regardless of these causes, such discrepancies stress the importance of beginning MEA optimization in parallel to catalyst development and highlight the challenges in extending advances in catalyst development to the technical system.[5] This particularly applies to unsupported materials, for which research on efficient CL design is at its infancy as compared

to their Pt-M/C counterparts. Moreover, to meet the U.S. DOE's target of 0.125 kW/g_{Pt}[109] by increasing the power output, fuel cells are operated at high current densities (> 1 A/cm^2_{MEA}), that imply cell potentials well below the 0.9 V_{RHE} at which ORR activity is assessed. Thus, an open debate has triggered regarding the adequacy of ORR activity values (i.e. current at 0.9 V_{RHE} in RDE experiments) as predictors of the performance at the high current densities relevant for efficient fuel cell operation. [5, 79]

4.3.1. Novel catalyst layer concepts

Conventional CLs (see section 4.1.) based on Pt-M/C catalysts are commonly prepared by processing the catalyst material into inks or pastes through addition of ionomer and water/alcohol, before applying these mixtures to either the membrane or GDL via spraying or coating techniques.[110] Naturally, similar processes were used for preparing CLs with unsupported Pt black catalysts from the 1950s until the 1980s; however the results obtained for this material will be discarded in this contribution due to the high loadings of ≈ 4 mg_{Pt}/cm^2_{MEA} typically used in those studies.[110]

The first promising PEFC experiments with unsupported catalysts, however, were conducted on CLs that were prepared by electrodeposition or sputter deposition of Pt onto the GDL.[89] Yet due to the limited ECSAs of < 10 m^2/g_{Pt}, the fuel cell performance of the resulting gas diffusion electrodes (GDE) could not match that of conventional Pt/C systems; for a summary of PEFC results on CLs prepared by sputtering the reader is referred to Ref. [89]. In the following, three examples of how researchers have achieved increased ECSA values and improved gas transport by increasing the CLs meso- and macroporosity will be presented.

Sievers et al. used an alternating sputtering approach of Pt and Co to create a CL matrix consisting of noble and non-noble metal domains.[111] The latter were mostly removed through dissolution during cell conditioning, leaving behind a mesoporous PtCo CL with improved mass-normalized performance at high current densities under H_2/air operation with respect to pure Pt CLs prepared by the same process. The macroporous Pt CLs with inverse opal structure on a GDL (as shown in **Figure 6f**) exhibits an ECSA amounting to 24 m^2/g_{Pt}, greatly exceeding the values of the first sputtered CLs.[66] The power densities in H_2/air operation exceeded those of conventional Pt/C systems, also owing to the unsupported CLs advantageous morphology, i.e. large void volume and interconnected macropores. In addition, the NSTF catalysts feature ECSAs of up to 17 m^2/g_{Pt} since the target metal is sputtered on a vertically aligned surface of crystalline organic whiskers (for details on the synthesis and characterization see section 2.2).[102] As NSTFs and their corresponding CLs are the most thoroughly investigated unsupported system up to date, they can serve as an instructive case study to highlight the challenges of optimizing CL, MEA and operation conditions.

NSTF-based MEAs are prepared by hotpressing the Pt-M sputtered whiskers onto the membrane, decreasing the whisker-whisker spacing and embedding them to ≈20 % of their length (0.5 μm) into the membrane. Under steady-state operation, NSTF catalysts have exceeded the performance of Pt/C electrodes, reaching inverse power densities of 0.16 g_{Pt}/kW and meeting the DOE's initial MA target of 0.44 A/mg_{Pt} at 0.9 V_{RHE}, as well as showing less than 40% activity loss after 30000 accelerated stress test cycles.[102, 112] Like the other systems mentioned above, NSTF CLs do not contain ionomer and rely on proton conduction via the extended Pt surface. However, since proton conductivity decreases significantly at low relative humidities (RHs),[105] implementation in an automotive PEFC stack would require a larger and expensive

humidification system, which is an important disadvantage vs. Pt-M/C CLs.[113] Additionally, under wet conditions (RH ≈ 100%) and temperatures below 60°C (occurring, e.g., upon car start-up) NSTF cathode CLs have a propensity to flooding, restricting the access to reactants and leading to cell reversal.[102, 113, 114] These observations prove the need for an efficient water management to improve the operational robustness of such systems. Indeed, efforts to increase the proton conductivity and the water removal capability by coating the whiskers' surface with ionomer were undertaken, yielding only minor improvement in high current density performance,[114] possibly due to the simultaneous increase in O_2 mass transport resistance.[102] Further strategies to mitigate this challenges include a dispersed catalyst/NSTF hybrid electrode, in which a Pt/C interlayer between whiskers and GDL serves as water storage and removal buffer,[114] and water removal through the anode by using differential pressures and thinner membranes.[102]

4.3.2. Classic catalyst layer concepts

Owing to the rapid progress in the synthesis of unsupported catalyst materials with well-defined and hierarchical structural motifs (cf. section 2), researchers are now working on implementing these materials in PEFCs, also using the classic approach to prepare CLs introduced in the section 4.3.1. Thereby, it is of utmost importance that the advantageous structure of the unsupported catalysts is not destroyed during processing and can be transferred to the catalyst layers. Ultimately this has to be investigated individually for different materials. However, in the studies cited in the following and our own experiments, no changes of the materials' structures were observed.

Recently, the group of Yamaguchi reported on the fuel cell performance of the hollow PtFe alloy nanocapsule electrocatalysts introduced in section 2.3 (**Figure 6d-e**).[36, 101] CLs (with a thickness of~1 μm) were prepared by dispersing the catalyst and Nafion ionomer (optimized ionomer-to-catalyst ratio ≈ 0.13) in a water/isopropanol mixture, followed by sonication and pulse spraying onto the membrane. Comparison of TEM images of the catalyst material before and after this processing step in references [36] and [101] indicates that the nanostructure is retained. Moreover, it was found that additional autoclaving of the ink for 24 h at 200°C leads to more uniform coverage and thinner ionomer films around the nanocapsules, correlating with significantly improved performance at high relative humidity (RH = 90 %) conditions. The authors explained this observation by the considerable swelling of the nonuniform, locally thick ionomer layers obtained without autoclaving at high RH conditions, which results in the blockage of the interspaces between the nanocapsules and limits oxygen diffusion. Further experiments indicated the presence of liquid water inside the CL under varying operation conditions, again highlighting the challenges of water removal and effective water management with such materials and thin CLs. Despite these shortcomings, the PtFe nanocapsule MEAs showed neither changes in the H_2/O_2 I/E curves nor ECSA loss after 10000 cycles of start-stop durability test (1.0 – 1.5 V_{RHE}, 500 mVs^{-1}), demonstrating the benefits of working with unsupported systems.[36, 101, 115]

Similar efforts have been undertaken by the group of Pivovar that works on the implementation of Pt-Ni nanowires (cf. Section 2.3) in real PEFCs. First tests showed significantly reduced ORR activities and ECSA values with respect to RDE data,[116] which can be related to significant Ni dissolution from the catalyst during break-in and conditioning, leading to ionomer poisoning effects.[108, 117, 118] Such poisoning suppresses the ORR on the Pt surface through a reorientation of the polymer network and causes reduced proton transport that affects high current density

performance.[119] Eventually, these shortcomings were mitigated by introducing two acid soaking steps of the MEA (15 hours, 0.01 M H_2SO_4, 20 °C) in the multi-step cell activation process.[108, 120] MEAs treated in this way show reduced Ni content, improved high current density performance plus increased ECSA and ORR activities, albeit the latter two are still significantly lower than the respective values from RDE studies.[120] Although further research on proton transport, oxygen transport and the cell activation process is needed to trigger performance improvements, PtNi nanowire CLs have already displayed superior performance to Pt/C in start-stop durability tests.[108]

Another successful demonstration of unsupported electrocatalysts, fct Pt-Fe nanotubes (cf. Section 2.3), was incorporated into ionomer free CLs by the spraying technique.[99] Under the PEFC test conditions in H_2/O_2 and H_2/air recommended by the DOE,[115] the fct PtFe nanotubes showed maximum power densities comparable to Pt/C systems and superior durability under accelerated degradation test conditions (potential of 1.4 V for 3 hours).

Regarding our own research on bimetallic aerogels, we presently work on transferring the Pt_3Ni aerogel catalyst to the PEFC. In brief, we have faced similar challenges as the authors mentioned above, i.e. low utilization of the catalyst (expressed as the quotient between PEFC- and RDE-measured values, $ECSA_{PEFC}/ECSA_{RDE}$), low ORR activity and poor high current density performance. For Pt_3Ni aerogel, these limitations were overcome by adding a filler material to the catalyst ink before preparation of the CL. Our progress is exemplified by the H_2/air I/E curves for Pt_3Ni aerogel and Pt/C benchmark MEAs in **Figure 9a** that feature comparable high current density performance. Details about the filler material and its effect will be disclosed in a forthcoming publication. Lastly, TEM images of the catalyst before and after processing into an

ink by ultrasonic dispersion (see **Figure 9b-c**) indicate that the unique aerogel structure can be transferred to the PEFC without damage.

5. Summary and Outlook

Progress in nanotechnology has promoted a growing interest in the rational design of unsupported metallic nanostructures for efficient catalysis of the ORR, which is a key reaction in PEFCs. Three representative types of unsupported electrocatalysts, namely metallic aerogels, nano/meso-structured thin films and template-derived nanostructures, were reviewed by demonstrating their design concept, synthesis procedure and structural features. In general, the self-supportability of these catalysts is derived from the mesoscale assembly/growth or structural engineering of nanomaterials while maintaining the nano-localized surface properties. Therefore, transferring the achievements in fine-tuned nanocatalysts into unsupported materials remains an important pursuit for designing application-oriented electrocatalysts. Taking metallic aerogels as an example, alloying, an extensively used strategy to enhance ORR performance of Pt-based catalysts, has been recently realized in the fabrication of $Pd_{80}Pt_{20}$, Pt_3Ni and Pt_3Cu aerogels that showed largely improved ORR activity and self-supportability. It has also been demonstrated that shape/structure effects (including core-shell structure, polyhedrons with controlled exposed facets, near-surface composition, etc.) often play an important role in tuning ORR catalysis on Pt-based nanocatalysts. These findings present challenges for the further exploration of the metal aerogel electrocatalysts with beneficial shape/structure/alloy effects. To fully implement these concepts, novel strategies for the synthesis (especially for the gelation/destabilization process) are highly needed. Although thin film catalysts with various compositions, particularly the 3M NSTF materials, have already been extensively studied with various compositions, further

investigations of templates with different structures or tuning the crystalline properties of the thin film by alloying would be possible future directions. Since unsupported catalysts from template synthesis often feature low dispersion of active sites, future efforts will be devoted to increase the ECSA and to control the exposed facets, as to improve the ORR activity.

Even though first efforts have been made to implement novel unsupported catalysts in the PEFC, the exploration of their behavior under fuel cell operating conditions is still necessary. To date, most of the catalyst testing is conducted in liquid half cells using the RDE technique because MEA fabrication and testing requires abundant material, expensive equipment and significant process optimization time. When the catalysts are transferred to the MEA, however, the catalyst layer has to provide mass/heat transfer and protonic/electronic transport besides catalyzing the ORR. This frequently results in a significant ORR activity mismatch between RDE and MEA experiments, which may in parts be due to the unoptimized MEA fabrication parameters. Thus, this illustrates the challenges in translating performance advancements from RDE studies to the technological application in PEFCs and highlights the need for further research on this process step. Fundamental advances in the understanding of optimal CL design are expected to pave the way to performance-oriented engineering of unsupported electrocatalysts implementable in the CLs of a technical MEA for PMFCs.

Acknowledgements

B.C. and S.H. contributed equally to this work. Financial supports from the Deutsche Forschungsgemeinschaft (DFG, EY16/18-1), the Swiss National Science Foundation (SNF, 20001E_151122/1), the European Research Council (ERC-2013-AdG AEROCAT) and the Bundesministerium für Bildung und Forschung (BMBF, FKZ 03SF0539) are gratefully acknowledged.

Received: ((will be filled in by the editorial staff))
Revised: ((will be filled in by the editorial staff))
Published online: ((will be filled in by the editorial staff))

Abbreviations

PEFC polymer electrolyte fuel cells
ORR oxygen reduction reaction
NP nanoparticle
NBB nano-sized building block
SEM scanning electron microscopy
TEM transmission electron microscopy
BET Brunauer−Emmett−Teller
HNS hollow nanosphere
MSTF meso-structured thin films
NSTF nano-structured thin films
DG double gyroid
1D one-dimensional
fct face-centered tetragonal
GDL gas diffusion layer
MEA membrane electrode assembly
ECSA electrochemical surface area
RDE rotating disk electrode
RHE reversible hydrogen electrode
DOE U.S. Department of Energy
MA mass-specific activity
SA surface-specific activity
GDL gas diffusion layer
CL catalyst layer
HOR hydrogen oxidation reaction
Pt-M alloy of platinum and non-noble metal
I/C ionomer-to-carbon-ratio
PFSA perfluorosulfonic acid
GDE gas diffusion electrodes
RH relative humidity

References

[1] S. Chu, Y. Cui, N. Liu, *Nat. Mater.* **2016**, *16*, 16.
[2] M. K. Debe, *Nature* **2012**, *486*, 43.
[3] V. R. Stamenkovic, D. Strmcnik, P. P. Lopes, N. M. Markovic, *Nat. Mater.* **2016**, *16*, 57.
[4] D. Li, H. Lv, Y. Kang, N. M. Markovic, V. R. Stamenkovic, *Annu. Rev. Chem. Biomol. Eng.* **2016**, *7*, 509.
[5] I. E. L. Stephens, J. Rossmeisl, I. Chorkendorff, *Science* **2016**, *354*, 1378.
[6] Z. W. Seh, J. Kibsgaard, C. F. Dickens, I. Chorkendorff, J. K. Norskov, T. F. Jaramillo, *Science* **2017**, *355*.
[7] M. Shao, Q. Chang, J. P. Dodelet, R. Chenitz, *Chem Rev* **2016**, *116*, 3594.
[8] Y. J. Wang, N. Zhao, B. Fang, H. Li, X. T. Bi, H. Wang, *Chem Rev* **2015**, *115*, 3433.
[9] Y. Nie, L. Li, Z. Wei, *Chem. Soc. Rev.* **2015**, *44*, 2168.

[10] H. A. Gasteiger, S. S. Kocha, B. Sompalli, F. T. Wagner, *Appl. Catal. B: Environ.* **2005**, *56*, 9.
[11] C. Chen, Y. Kang, Z. Huo, Z. Zhu, W. Huang, H. L. Xin, J. D. Snyder, D. Li, J. A. Herron, M. Mavrikakis, M. Chi, K. L. More, Y. Li, N. M. Markovic, G. A. Somorjai, P. Yang, V. R. Stamenkovic, *Science* **2014**, *343*, 1339.
[12] M. Escudero-Escribano, P. Malacrida, M. H. Hansen, U. G. Vej-Hansen, A. Velazquez-Palenzuela, V. Tripkovic, J. Schiotz, J. Rossmeisl, I. E. Stephens, I. Chorkendorff, *Science* **2016**, *352*, 73.
[13] L. Bu, N. Zhang, S. Guo, X. Zhang, J. Li, J. Yao, T. Wu, G. Lu, J. Y. Ma, D. Su, X. Huang, *Science* **2016**, *354*, 1410.
[14] G. Wu, K. L. More, C. M. Johnston, P. Zelenay, *Science* **2011**, *332*, 443.
[15] J. Zhang, Z. Zhao, Z. Xia, L. Dai, *Nat Nanotechnol* **2015**, *10*, 444.
[16] R. Silva, D. Voiry, M. Chhowalla, T. Asefa, *J. Am. Chem. Soc.* **2013**, *135*, 7823.
[17] S. Guo, S. Zhang, S. Sun, *Angew. Chem. Int. Ed.* **2013**, *52*, 8526.
[18] C. Zhang, S. Y. Hwang, A. Trout, Z. Peng, *J. Am. Chem. Soc.* **2014**, *136*, 7805.
[19] T. Y. Ma, S. Dai, S. Z. Qiao, *Materials Today* **2016**, *19*, 265.
[20] J. Speder, A. Zana, I. Spanos, J. J. K. Kirkensgaard, K. Mortensen, M. Hanzlik, M. Arenz, *J. Power Sources* **2014**, *261*, 14.
[21] O. Gröger, H. A. Gasteiger, J. P. Suchsland, *J. Electrochem. Soc* **2015**, *162*, A2605.
[22] T. Mittermeier, A. Weiß, F. Hasché, G. Hübner, H. A. Gasteiger, *J. Electrochem. Soc* **2016**, *164*, F127.
[23] C. Zhu, D. Du, A. Eychmuller, Y. Lin, *Chem Rev* **2015**, *115*, 8896.
[24] Y. Wang, K. S. Chen, J. Mishler, S. C. Cho, X. C. Adroher, *Applied Energy* **2011**, *88*, 981.
[25] W. Liu, P. Rodriguez, L. Borchardt, A. Foelske, J. Yuan, A. K. Herrmann, D. Geiger, Z. Zheng, S. Kaskel, N. Gaponik, R. Kotz, T. J. Schmidt, A. Eychmuller, *Angew. Chem. Int. Ed.* **2013**, *52*, 9849.
[26] S. Henning, L. Kuhn, J. Herranz, J. Durst, T. Binninger, M. Nachtegaal, M. Werheid, W. Liu, M. Adam, S. Kaskel, A. Eychmuller, T. J. Schmidt, *J. Electrochem. Soc.* **2016**, *163*, F998.
[27] S. Henning, L. Kühn, J. Herranz, M. Nachtegaal, R. Hübner, M. Werheid, A. Eychmüller, T. J. Schmidt, *Submitted to Electrochim. Acta*.
[28] D. van der Vliet, C. Wang, M. Debe, R. Atanasoski, N. M. Markovic, V. R. Stamenkovic, *Electrochimica Acta* **2011**, *56*, 8695.
[29] D. F. van der Vliet, C. Wang, D. Tripkovic, D. Strmcnik, X. F. Zhang, M. K. Debe, R. T. Atanasoski, N. M. Markovic, V. R. Stamenkovic, *Nature materials* **2012**, *11*, 1051.
[30] M. K. Debe, *J. Electrochem. Soc.* **2013**, *160*, F522.
[31] J. Kibsgaard, Y. Gorlin, Z. Chen, T. F. Jaramillo, *J. Am. Chem. Soc.* **2012**, *134*, 7758.
[32] S. M. Alia, K. O. Jensen, B. S. Pivovar, Y. Yan, *ACS Catal.* **2012**, *2*, 858.
[33] S. M. Alia, K. Jensen, C. Contreras, F. Garzon, B. Pivovar, Y. Yan, *ACS Catal.* **2013**, *3*, 358.
[34] S. M. Alia, S. Pylypenko, K. C. Neyerlin, D. A. Cullen, S. S. Kocha, B. S. Pivovar, *ACS Catal.* **2014**, *4*, 2680.
[35] J. Lee, J. M. Yoo, Y. Ye, Y. Mun, S. Lee, O. H. Kim, H. W. Rhee, H. I. Lee, Y. E. Sung, J. Lee, *Adv. Energy Mater.* **2015**, *5*, 1402093.
[36] T. Tamaki, H. Kuroki, S. Ogura, T. Fuchigami, Y. Kitamoto, T. Yamaguchi, *Energy Environ. Sci.* **2015**, *8*, 3545.

[37] W. Liu, A. K. Herrmann, N. C. Bigall, P. Rodriguez, D. Wen, M. Oezaslan, T. J. Schmidt, N. Gaponik, A. Eychmuller, *Acc. Chem. Res.* **2015**, *48*, 154.
[38] W. Liu, A. K. Herrmann, D. Geiger, L. Borchardt, F. Simon, S. Kaskel, N. Gaponik, A. Eychmuller, *Angew. Chem. Int. Ed.* **2012**, *51*, 5743.
[39] D. Wen, W. Liu, D. Haubold, C. Zhu, M. Oschatz, M. Holzschuh, A. Wolf, F. Simon, S. Kaskel, A. Eychmuller, *ACS Nano* **2016**, *10*, 2559.
[40] M. Oezaslan, W. Liu, M. Nachtegaal, A. I. Frenkel, B. Rutkowski, M. Werheid, A. K. Herrmann, C. Laugier-Bonnaud, H. C. Yilmaz, N. Gaponik, A. Czyrska-Filemonowicz, A. Eychmuller, T. J. Schmidt, *Phys. Chem. Chem. Phys.* **2016**, *18*, 20640.
[41] B. Cai, D. Wen, W. Liu, A. K. Herrmann, A. Benad, A. Eychmuller, *Angew. Chem. Int. Ed.* **2015**, *54*, 13101.
[42] B. Cai, A. Dianat, R. Hubner, W. Liu, D. Wen, A. Benad, L. Sonntag, T. Gemming, G. Cuniberti, A. Eychmuller, *Adv. Mater.* **2017**, *29*, 1605254.
[43] W. Liu, D. Haubold, B. Rutkowski, M. Oschatz, R. Hubner, M. Werheid, C. Ziegler, L. Sonntag, S. H. Liu, Z. K. Zheng, A. K. Herrmann, D. Geiger, B. Terlan, T. Gemming, L. Borchardt, S. Kaskel, A. Czyrska-Filemonowicz, A. Eychmuller, *Chem. Mater.* **2016**, *28*, 6477.
[44] N. Gaponik, A.-K. Herrmann, A. Eychmüller, *J. Phys. Chem. Lett.* **2011**, *3*, 8.
[45] A. K. Herrmann, P. Formanek, L. Borchardt, M. Klose, L. Giebeler, J. Eckert, S. Kaskel, N. Gaponik, A. Eychmuller, *Chem. Mater.* **2014**, *26*, 1074.
[46] N. C. Bigall, A. K. Herrmann, M. Vogel, M. Rose, P. Simon, W. Carrillo-Cabrera, D. Dorfs, S. Kaskel, N. Gaponik, A. Eychmuller, *Angew. Chem. Int. Ed.* **2009**, *48*, 9731.
[47] D. Wen, A. K. Herrmann, L. Borchardt, F. Simon, W. Liu, S. Kaskel, A. Eychmuller, *J. Am. Chem. Soc.* **2014**, *136*, 2727.
[48] H. You, S. Yang, B. Ding, H. Yang, *Chem. Soc. Rev.* **2013**, *42*, 2880.
[49] C. Zhu, Q. Shi, S. Fu, J. Song, H. Xia, D. Du, Y. Lin, *Adv. Mater.* **2016**, *28*, 8779.
[50] L. Kuhn, A. K. Herrmann, B. Rutkowski, M. Oezaslan, M. Nachtegaal, M. Klose, L. Giebeler, N. Gaponik, J. Eckert, T. J. Schmidt, A. Czyrska-Filemonowicz, A. Eychmuller, *Chem. Eur. J.* **2016**, *22*, 13446.
[51] D. R. Rolison, *Science* **2003**, *299*, 1698.
[52] K. G. S. Ranmohotti, X. N. Gao, I. U. Arachchige, *Chem. Mater.* **2013**, *25*, 3528.
[53] X. Gao, R. J. Esteves, T. T. Luong, R. Jaini, I. U. Arachchige, *J. Am. Chem. Soc.* **2014**, *136*, 7993.
[54] M. K. Debe, R. T. Atanasoski, A. J. Steinbach, *ECS Trans.* **2011**, *41*, 937.
[55] M. K. Debe, *ECS Trans.* **2012**, *45*, 47.
[56] M. K. Debe, A. K. Schmoeckel, G. D. Vernstrom, R. Atanasoski, *J. Power Sources* **2006**, *161*, 1002.
[57] N. N. Kariuki, W. J. Khudhayer, T. Karabacak, D. J. Myers, *ACS Catal.* **2013**, *3*, 3123.
[58] J. Kibsgaard, A. Jackson, T. F. Jaramillo, *Nano Energy* **2016**, *29*, 243.
[59] Y. Liu, J. Goebl, Y. Yin, *Chem. Soc. Rev.* **2013**, *42*, 2610.
[60] A. B. Papandrew, R. W. Atkinson, G. A. Goenaga, S. S. Kocha, J. W. Zack, B. S. Pivovar, T. A. Zawodzinski, *J. Electrochem. Soc.* **2013**, *160*, F848.
[61] S. M. Alia, Y. S. Yan, B. S. Pivovar, *Catal. Sci. Technol.* **2014**, *4*, 3589.
[62] Z. Chen, M. Waje, W. Li, Y. Yan, *Angew. Chem. Int. Ed.* **2007**, *46*, 4060.
[63] S. M. Alia, G. Zhang, D. Kisailus, D. Li, S. Gu, K. Jensen, Y. Yan, *Adv. Funct. Mater.* **2010**, *20*, 3742.

[64] S. M. Alia, B. A. Larsen, S. Pylypenko, D. A. Cullen, D. R. Diercks, K. C. Neyerlin, S. S. Kocha, B. S. Pivovar, *ACS Catal.* **2014**, *4*, 1114.
[65] S. M. Alia, S. Pylypenko, A. Dameron, K. C. Neyerlin, S. S. Kocha, B. S. Pivovar, *J. Electrochem. Soc.* **2016**, *163*, F296.
[66] O.-H. Kim, Y.-H. Cho, S. H. Kang, H.-Y. Park, M. Kim, J. W. Lim, D. Y. Chung, M. J. Lee, H. Choe, Y.-E. Sung, *Nat. Comm.* **2013**, *4*, 2473.
[67] T. J. Schmidt, H. A. Gasteiger, R. J. Behm, *J. Electrochem. Soc.* **1999**, *146*, 1296.
[68] K. Shinozaki, J. W. Zack, R. M. Richards, B. S. Pivovar, S. S. Kocha, *Journal of The Electrochemical Society* **2015**, *162*, F1144.
[69] K. Shinozaki, J. W. Zack, S. Pylypenko, B. S. Pivovar, S. S. Kocha, *J. Electrochem. Soc.* **2015**, *162*, F1384.
[70] Y. Garsany, J. Ge, J. St-Pierre, R. Rocheleau, K. E. Swider-Lyons, *J. Electrochem. Soc.* **2014**, *161*, F628.
[71] S. Kocha, *2014 DOE Hydrogen and Fuel Cells Program Review. https://www.hydrogen.energy.gov/pdfs/progress14/v_m_1_kocha_2014.pdf*.
[72] U. A. Paulus, T. J. Schmidt, H. A. Gasteiger, R. J. Behm, *J. Electroanal. Chem.* **2001**, *495*, 134.
[73] V. Stamenkovic, B. S. Mun, K. J. Mayrhofer, P. N. Ross, N. M. Markovic, J. Rossmeisl, J. Greeley, J. K. Norskov, *Angew. Chem. Int. Ed.* **2006**, *45*, 2897.
[74] J. Greeley, I. E. Stephens, A. S. Bondarenko, T. P. Johansson, H. A. Hansen, T. F. Jaramillo, J. Rossmeisl, I. Chorkendorff, J. K. Norskov, *Nat. Chem.* **2009**, *1*, 552.
[75] L. Gan, M. Heggen, S. Rudi, P. Strasser, *Nano Letters* **2012**, *12*, 5423.
[76] B. H. Han, C. E. Carlton, A. Kongkanand, R. S. Kukreja, B. R. Theobald, L. Gan, R. O'Malley, P. Strasser, F. T. Wagner, Y. Shao-Horn, *Energ. Environ. Sci.* **2015**, *8*, 258.
[77] R. Wang, C. Xu, X. Bi, Y. Ding, *Energy Environ. Sci.* **2012**, *5*, 5281.
[78] K. Shinozaki, Y. Morimoto, B. S. Pivovar, S. S. Kocha, *Electrochim. Acta* **2016**, *213*, 783.
[79] A. Kongkanand, M. F. Mathias, *J Phys Chem Lett* **2016**, *7*, 1127.
[80] S. Fu, C. Zhu, J. Song, M. H. Engelhard, H. Xia, D. Du, Y. Lin, *ACS Appl Mater Interfaces* **2016**, *8*, 35213.
[81] Y. G. Zhu, Y. Wang, Y. M. Shi, Z. X. Huang, L. Fu, H. Y. Yang, *Adv. Energy Mater.* **2014**, *4*, DOI: 10.1002/aenm.201301788.
[82] A. Forner-Cuenca, J. Biesdorf, L. Gubler, P. M. Kristiansen, T. J. Schmidt, P. Boillat, *Advanced materials* **2015**, *27*, 6317.
[83] A. El-Kharouf, N. V. Rees, R. Steinberger-Wilckens, *Fuel Cells* **2014**, *14*, 735.
[84] B. Andreaus, M. Eikerling, in *Device and Materials Modeling in PEM Fuel Cells*, (Eds: S. J. Paddison, K. S. Promislow), Springer New York, New York, NY 2009, 41.
[85] K. Kojima, K. Fukazawa, *ECS Transactions* **2015**, *69*, 213.
[86] K. C. Neyerlin, W. Gu, J. Jorne, A. Clark, H. A. Gasteiger, *J. Electrochem. Soc* **2007**, *154*, B279.
[87] A. Ohma, T. Mashio, K. Sato, H. Iden, Y. Ono, K. Sakai, K. Akizuki, S. Takaichi, K. Shinohara, *Electrochimica Acta* **2011**, *56*, 10832.
[88] A. Pătru, A. Rabis, S. E. Temmel, R. Kotz, T. J. Schmidt, *Catalysis Today* **2016**, *262*, 161.
[89] B. Schwanitz, A. Rabis, M. Horisberger, G. G. Scherer, T. J. Schmidt, *Chimia* **2012**, *66*, 110.
[90] A. Rabis, P. Rodriguez, T. J. Schmidt, *ACS Catalysis* **2012**, *2*, 864.

[91] H. A. Gasteiger, W. Gu, R. Makharia, M. F. Mathias, B. Sompalli, in *Handbook of Fuel Cells*, John Wiley & Sons, Ltd, 2010.
[92] T. Soboleva, X. Zhao, K. Malek, Z. Xie, T. Navessin, S. Holdcroft, *ACS applied materials & interfaces* **2010**, *2*, 375.
[93] K. More, R. Borup, K. Reeves, *ECS Trans.* **2006**, *3*, 717.
[94] T. Soboleva, K. Malek, Z. Xie, T. Navessin, S. Holdcroft, *ACS Appl Mater Interfaces* **2011**, *3*, 1827.
[95] S. Holdcroft, *Chem Mater* **2014**, *26*, 381.
[96] S. Thiele, T. Fürstenhaupt, D. Banham, T. Hutzenlaub, V. Birss, C. Ziegler, R. Zengerle, *Journal of Power Sources* **2013**, *228*, 185.
[97] N. Nonoyama, S. Okazaki, A. Z. Weber, Y. Ikogi, T. Yoshida, *J. Electrochem. Soc* **2011**, *158*, B416.
[98] W. Gu, D. R. Baker, Y. Liu, H. A. Gasteiger, in *Handbook of Fuel Cells*, John Wiley & Sons, Ltd, 2010.
[99] J. Lee, J. M. Yoo, Y. Ye, Y. Mun, S. Lee, O.-H. Kim, H.-W. Rhee, H. I. Lee, Y.-E. Sung, J. Lee, *Adv. Energy Mater.* **2015**, *5*, 1402093.
[100] M. H. Eikerling, K. Malek, Q. Wang, in *PEM Fuel Cell Electrocatalysts and Catalyst Layers: Fundamentals and Applications*, (Ed: J. Zhang), Springer London, London 2008, 381.
[101] H. Kuroki, T. Tamaki, T. Yamaguchi, *J. Electrochem. Soc* **2016**, *163*, F927.
[102] M. K. Debe, *J Electrochem Soc* **2013**, *160*, F522.
[103] U. A. Paulus, Z. Veziridis, B. Schnyder, M. Kuhnke, G. G. Scherer, A. Wokaun, *J. Electroanal. Chem.* **2003**, *541*, 77.
[104] L. Hu, M. Zhang, S. Komini Babu, S. Litster, *ECS Transactions* **2016**, *75*, 339.
[105] P. K. Sinha, W. Gu, A. Kongkanand, E. Thompson, *J. Electrochem. Soc* **2011**, *158*, B831.
[106] C. Chen, Y. Kang, Z. Huo, Z. Zhu, W. Huang, H. L. Xin, J. D. Snyder, D. Li, J. A. Herron, M. Mavrikakis, M. Chi, K. L. More, Y. Li, N. M. Markovic, G. A. Somorjai, P. Yang, V. R. Stamenkovic, *Science* **2014**, *343*, 1339.
[107] V. Stamenkovic, *2015 DOE Hydrogen and Fuel Cells Program Review: Nanosegregated Cathode Catalysts with Ultra Low Platinu*.
[108] B. Pivovar, *2015 DOE Hydrogen and Fuel Cells Program Review:Extended, Continuous Pt Nanostructures in Thick, Dis*.
[109] DOE, *Fuel Cell Multi-Year Research, Develo*.
[110] S. S. Kocha, *Handboof of Fuel Cells: Principles of MEA preparation* **2010**.
[111] G. Sievers, S. Mueller, A. Quade, F. Steffen, S. Jakubith, A. Kruth, V. Brueser, *Journal of Power Sources* **2014**, *268*, 255.
[112] A. J. Steinbach, *2016 DOE Hydrogen and Fuel Cells Program Review: Highly Active, Durable, and Ultra-low PGM NSTF Thin Film ORR Catalysts and Supports (U.S. Department of Energy, 2016).*
[113] A. Kongkanand, J. E. Owejan, S. Moose, M. Dioguardi, M. Biradar, R. Makharia, *J. Electrochem. Soc.* **2012**, *159*, F676.
[114] A. Kongkanand, M. Dioguardi, C. Ji, E. L. Thompson, *J. Electrochem. Soc.* **2012**, *159*, F405.
[115] D. Papageorgopoulos, *DOE's 2015 Annual Merit Review and Peer Evaluation Meeting: Fuel Cells Program – Plenary Presentation http://www.hydrogen.energy.gov/pdfs/review15/fc000_papageorgopoulos_2015_o.pdf*.

[116] S. A. Mauger, K. C. Neyerlin, S. M. Alia, K. Hurst, S. Shulda, C. Ngo, J. N. Weker, S. Pylypenko, B. S. Pivovar, *ECS Prime 2016, Oral Presentation 2447, https://ecs.confex.com/ecs/230/webprogram/Paper93933.html*.
[117] T. A. Greszler, T. E. Moylan, H. A. Gasteiger, in *Handbook of Fuel Cells*, John Wiley & Sons, Ltd, 2010.
[118] B. Kienitz, B. Pivovar, T. Zawodzinski, F. H. Garzon, *J. Electrochem. Soc.* **2011**, *158*, B1175.
[119] T. Okada, in *Handbook of Fuel Cells*, John Wiley & Sons, Ltd, 2010.
[120] B. Pivovar, *2016 DOE Hydrogen and Fuel Cells Program Review: Extended Surface Electrocatalyst Development (U.S. Department of Energy, 20*.

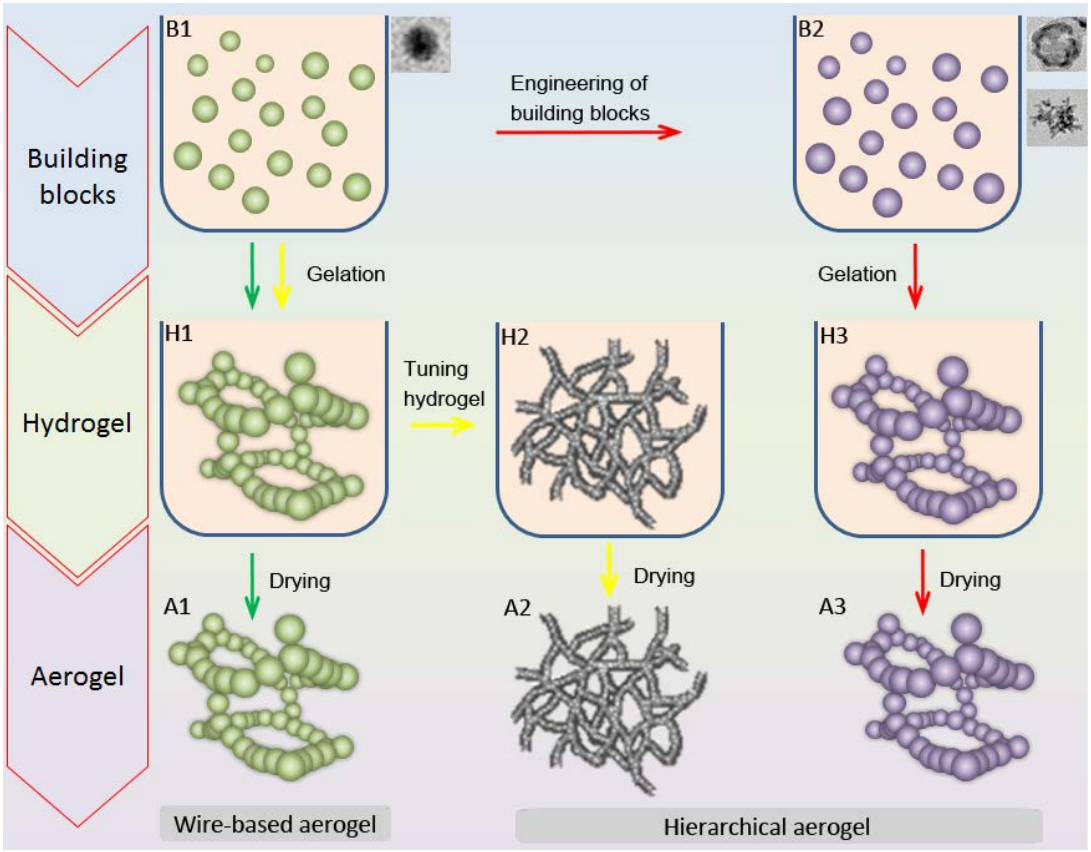

Figure 1. Schematic illustration of the synthesis procedures of noble metal-based aerogels via sol-gel processes. In general, there are three steps, including preparation of NBBs, gelation to hydrogel and supercritical drying to aerogel. Depending on the engineering of each selected step, the strategies can be divided into three and lead to different structures. Green arrows: Strategy I (B1-H1-A1); Yellow arrows: Strategy II (B1-H1-H2-A2); Red arrows: strategy III (B1-B2-H3-A3). The spontaneous gelation method which belongs to Strategy I can exempt the B1 step, where hydrogels were formed directly via the reduction of metal precursors. The TEM images next to B1 and B2 are examples of the NBBs.

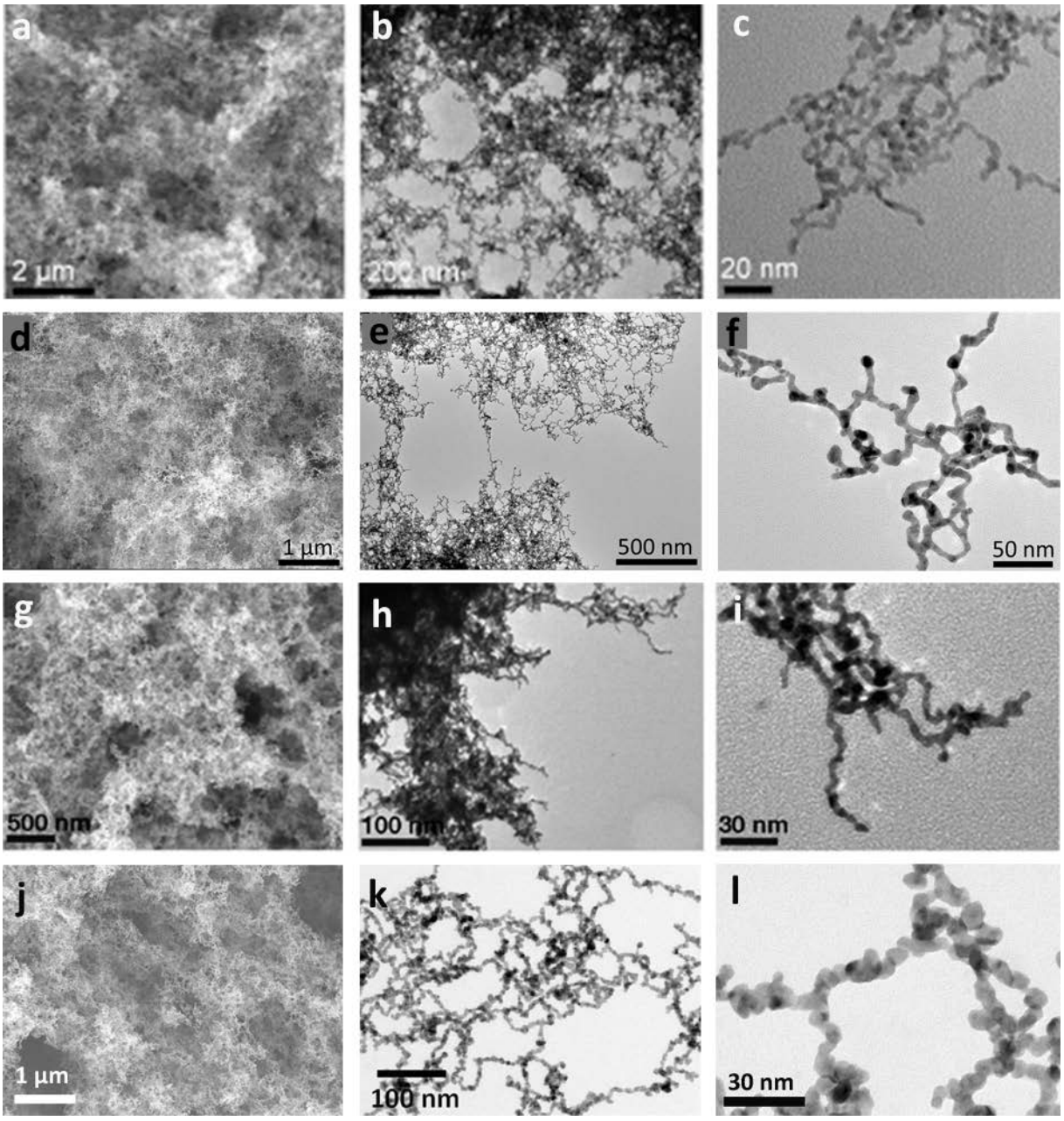

Figure 2. SEM and TEM images of some representative wire-based mono/bimetallic aerogels. a-c) Pd aerogels. Reproduced with permission.[38] Copyright 2012, Wiley-VCH. d-f) Au aerogels. Reproduced with permission.[39] Copyright 2016, American Chemical Society. g-h) $Pd_{50}Pt_{50}$ aerogels. Reproduced with permission.[25] Copyright 2013, Wiley-VCH. j-l) Pt_3Ni aerogels.[26]

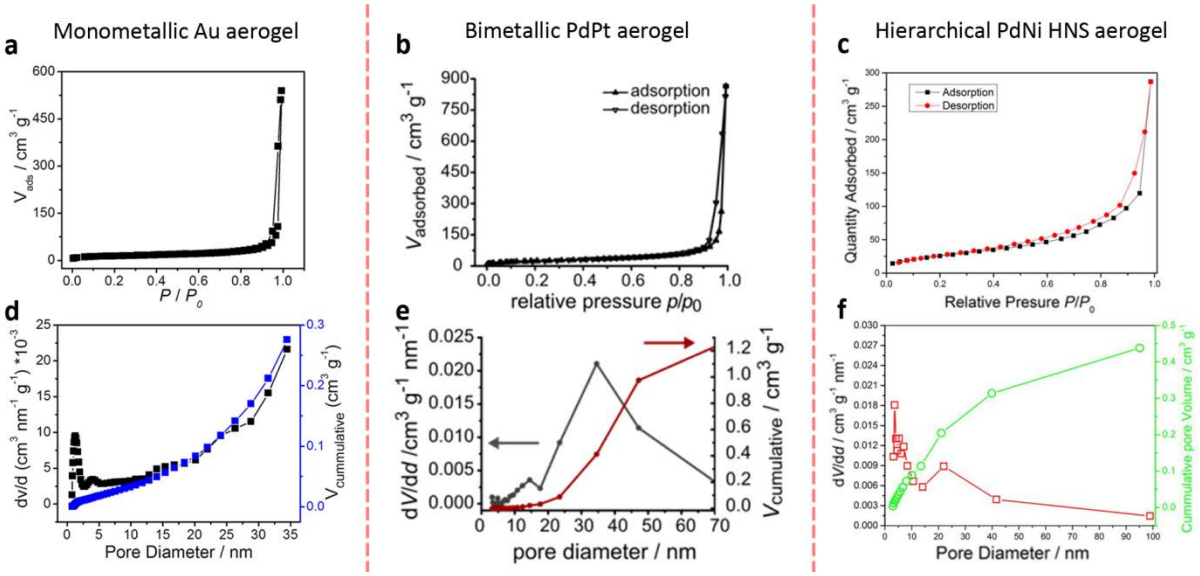

Figure 3. Nitrogen physisorption isotherms, pore size distributions, and cumulative pore volumes ($V_{cumulative}$) of different metallic aerogels. a,d) Monometallic Au aerogels. Reproduced with permission.[39] Copyright 2016, American Chemical Society. b,e) Bimetallic PdPt aerogels. Reproduced with permission.[37] Copyright 2015, American Chemical Society. c,f) Hierarchical PdNi HNS aerogels. Reproduced with permission.[41] Copyright 2015, Wiley-VCH.

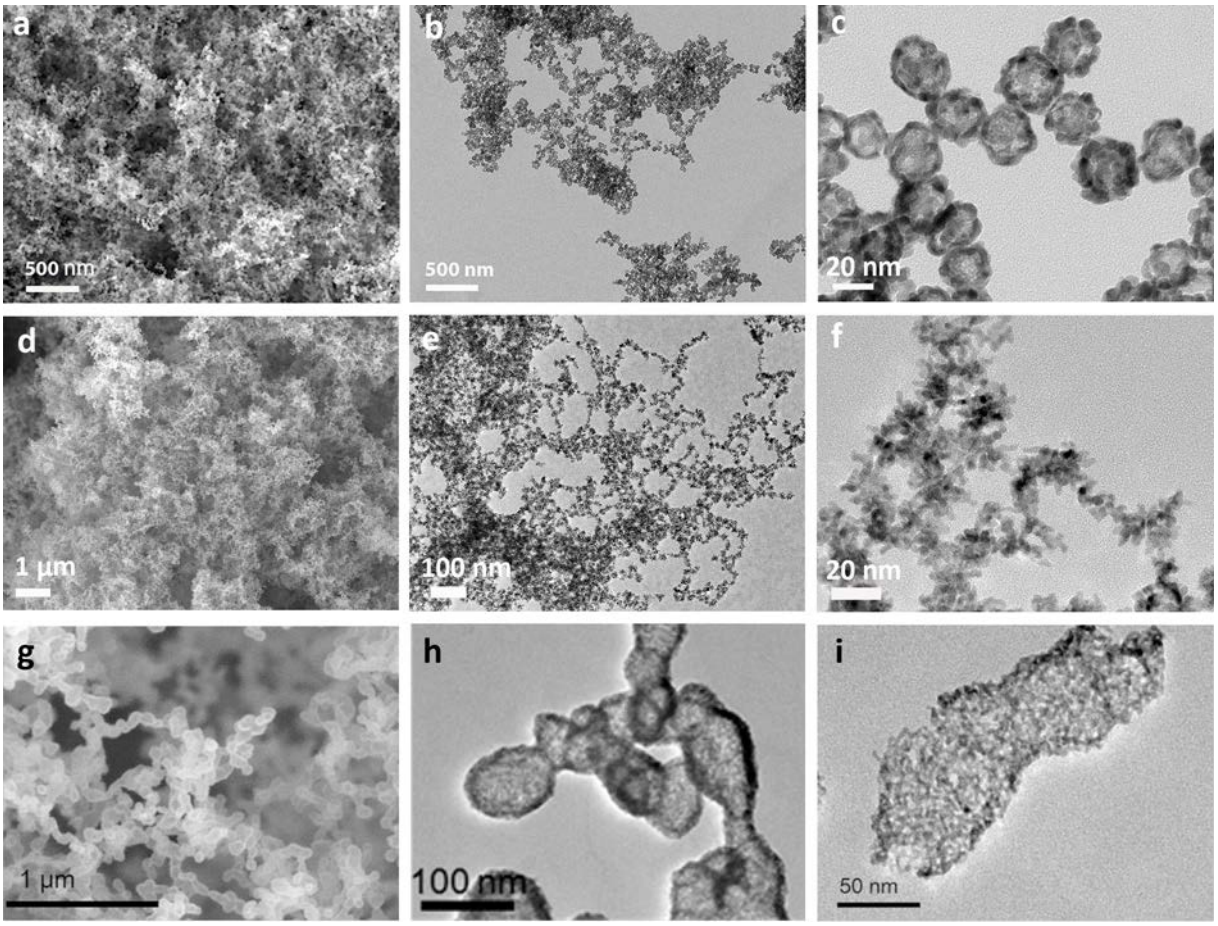

Figure 4. SEM and TEM images of the hierarchical aerogels: a-c) Pd-Ni hollow nanospheres aerogel from Strategy III. Reproduced with permission.[41] Copyright 2015, Wiley-VCH. d-f) Pt-Ni dendritic aerogel from Strategy III. Reproduced with permission.[42] Copyright 2017, Wiley-VCH. g-i) PtAg nanotubular aerogel from Strategy II. Reproduced with permission.[43] Copyright 2016, American Chemical Society.

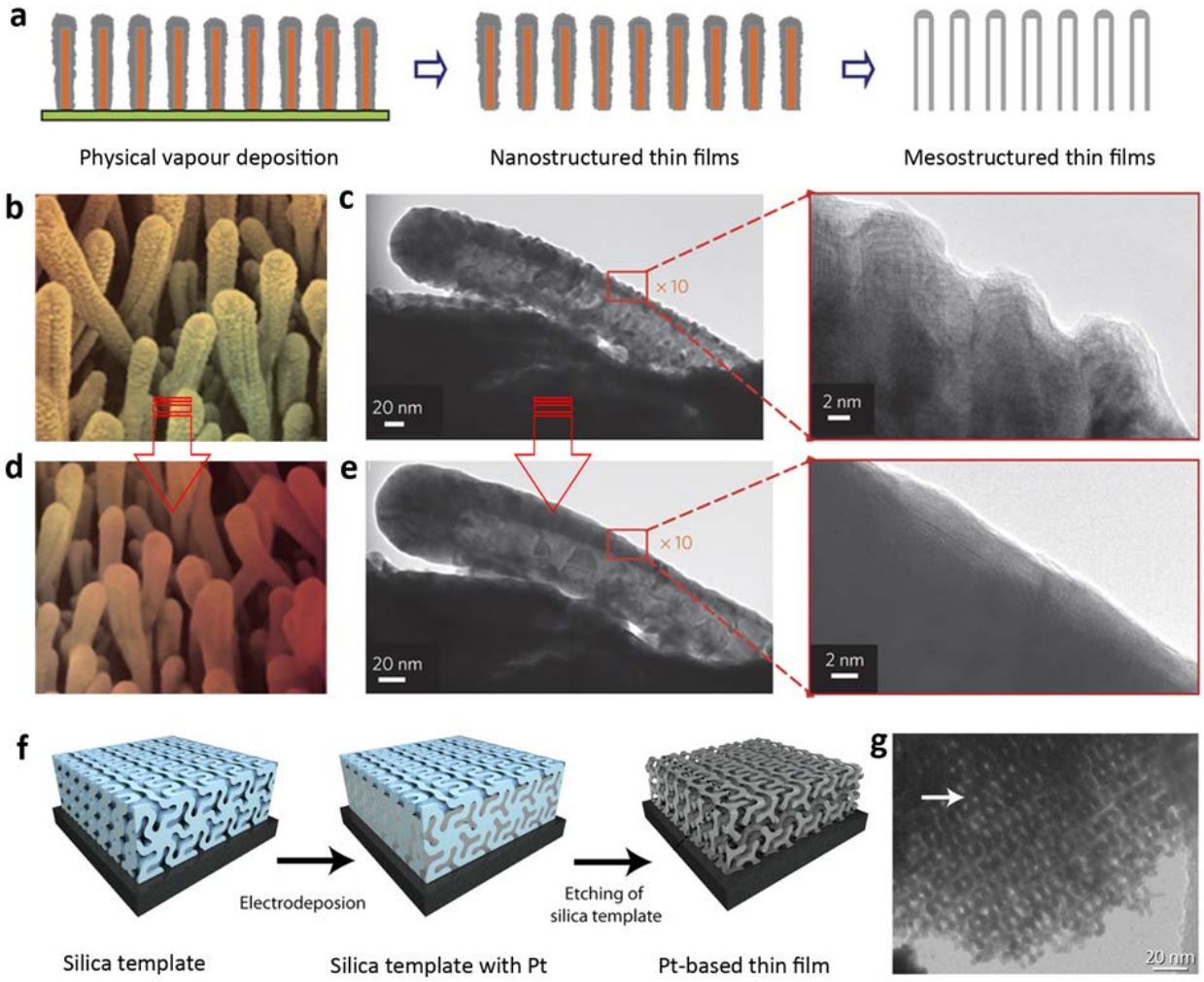

Figure 5. a) Schematic illustration of the preparation of NSTFs and their transformation to MSTFs. High-resolution SEM images of b) NSTF and d) MSTF. In situ TEM analysis during the transformation from c) NSTF to e) MSTF by annealing at 400 °C in reductive atmosphere. Reproduced with permission.[29] Copyright 2012, Nature Publishing Group. f) Schematic synthesis procedure for Pt or Pt-alloy mesoporous double gyroid thin films by electrodeposition on a silica template. Reproduced with permission.[58] Copyright 2016, Elsevier. g) TEM image of the Pt mesoporous double gyroid thin film. Reproduced with permission.[31] Copyright 2012, American Chemical Society.

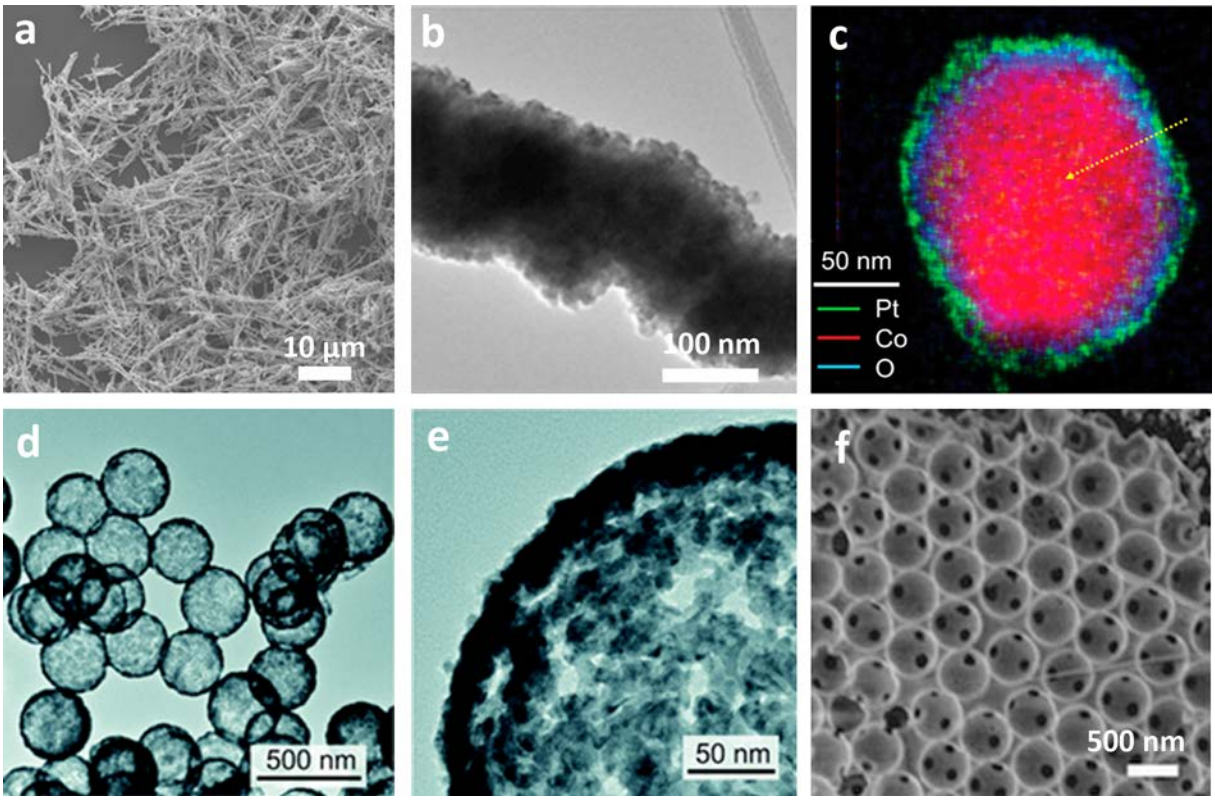

Figure 6. a) SEM, b) TEM and c) energy-dispersive X-ray spectrum images of a cross-section of the Pt-coated Co nanowires. Reproduced with permission.[34] Copyright 2014, American Chemical Society. d-e) TEM images of the connected Pt–Fe catalysts with a porous hollow capsule structure. Reproduced with permission.[36] Copyright 2015, Royal Society of Chemistry. f) SEM image of an inverse-opal Pt electrode surface prepared by electrodeposition using a self-assembled polystyrene template. Reproduced with permission.[66] Copyright 2013, Nature Publishing Group.

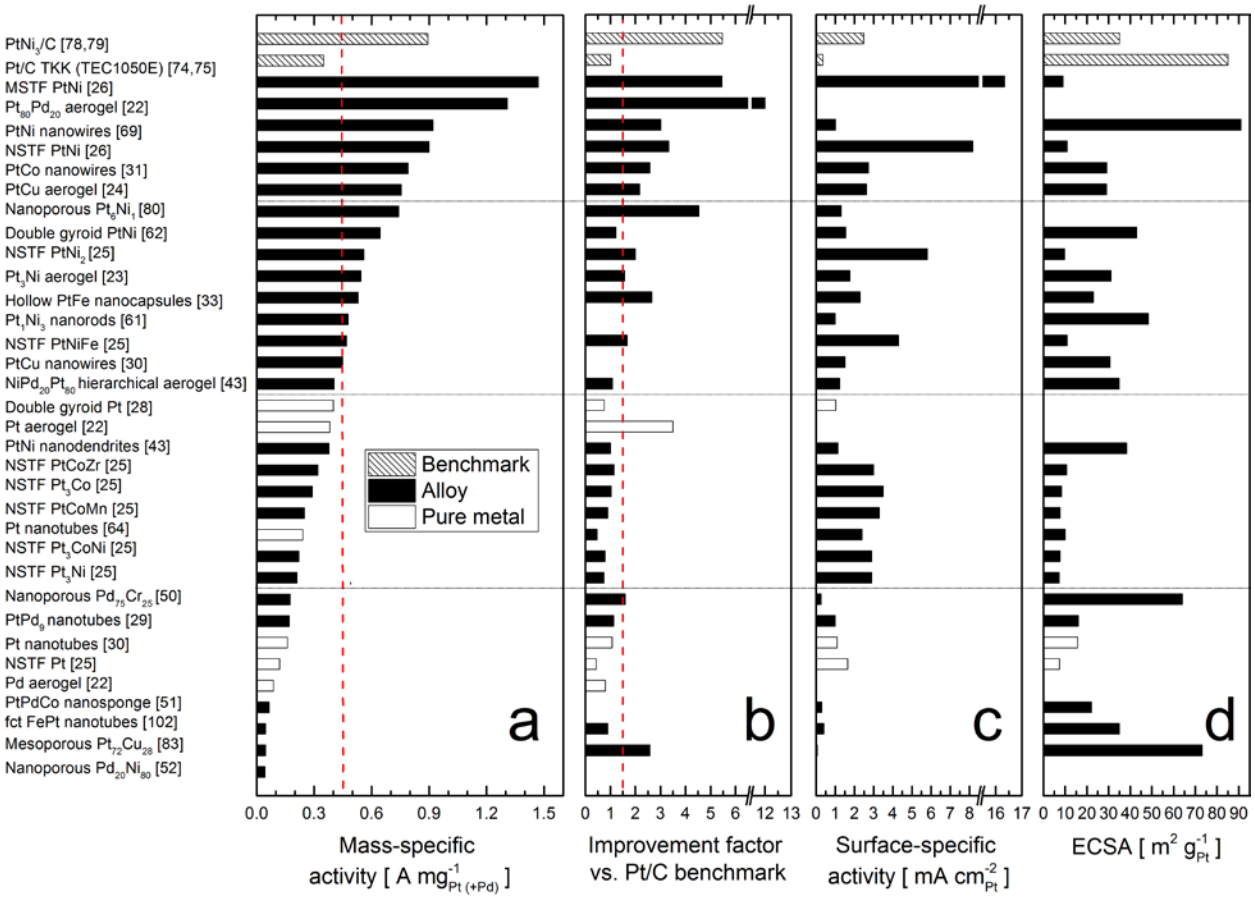

Figure 7. a) Overview of mass-specific ORR activity, b) corresponding improvement factor *vs*. Pt/C benchmark used in the same study, c) surface-specific ORR activity and d) ECSA for unsupported catalysts derived from liquid half cell (RDE) experiments. Activity values are stated at 0.9 V_{RHE} in O_2-saturated 0.1 M $HClO_4$ electrolyte, following adaption of some reported values as specified in the main text and were normalized to Pt or total Pt and Pd contents (where applicable). The red dotted line in a illustrates the DOE MA target of 0.44 A/mg_{Pt}[21]; the line in b corresponds to an ORR activity improvement factor of 1.5. State-of-the art Pt/C and Pt alloy/C catalysts are included as benchmarks at the top of the chart and blank spaces correspond to missing data that was not provided in the references.

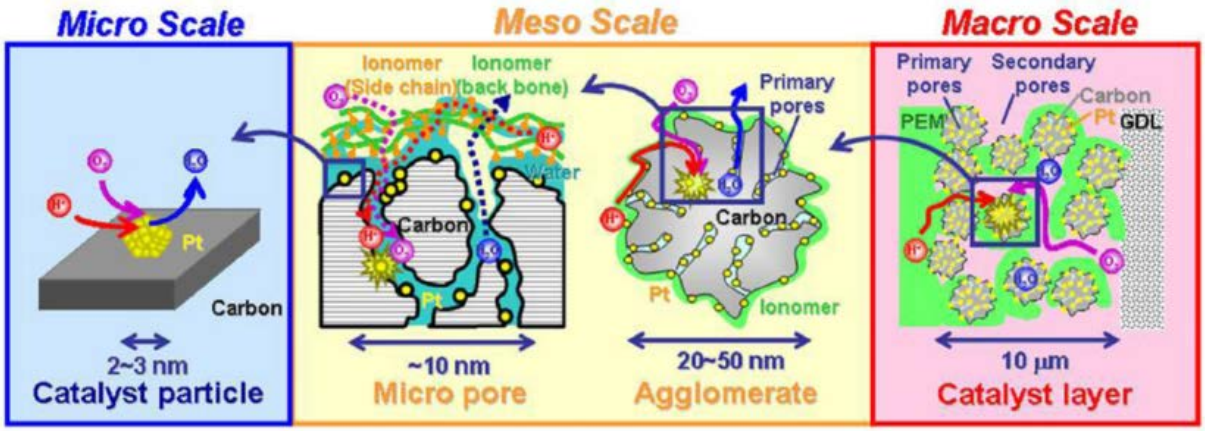

Figure 8. Different scales of the catalyst layer, highlighting relevant processes and structural features. The red, purple and blue circles represent protons, oxygen and water, respectively. Reproduced with permission.[87] Copyright 2011, Elsevier.

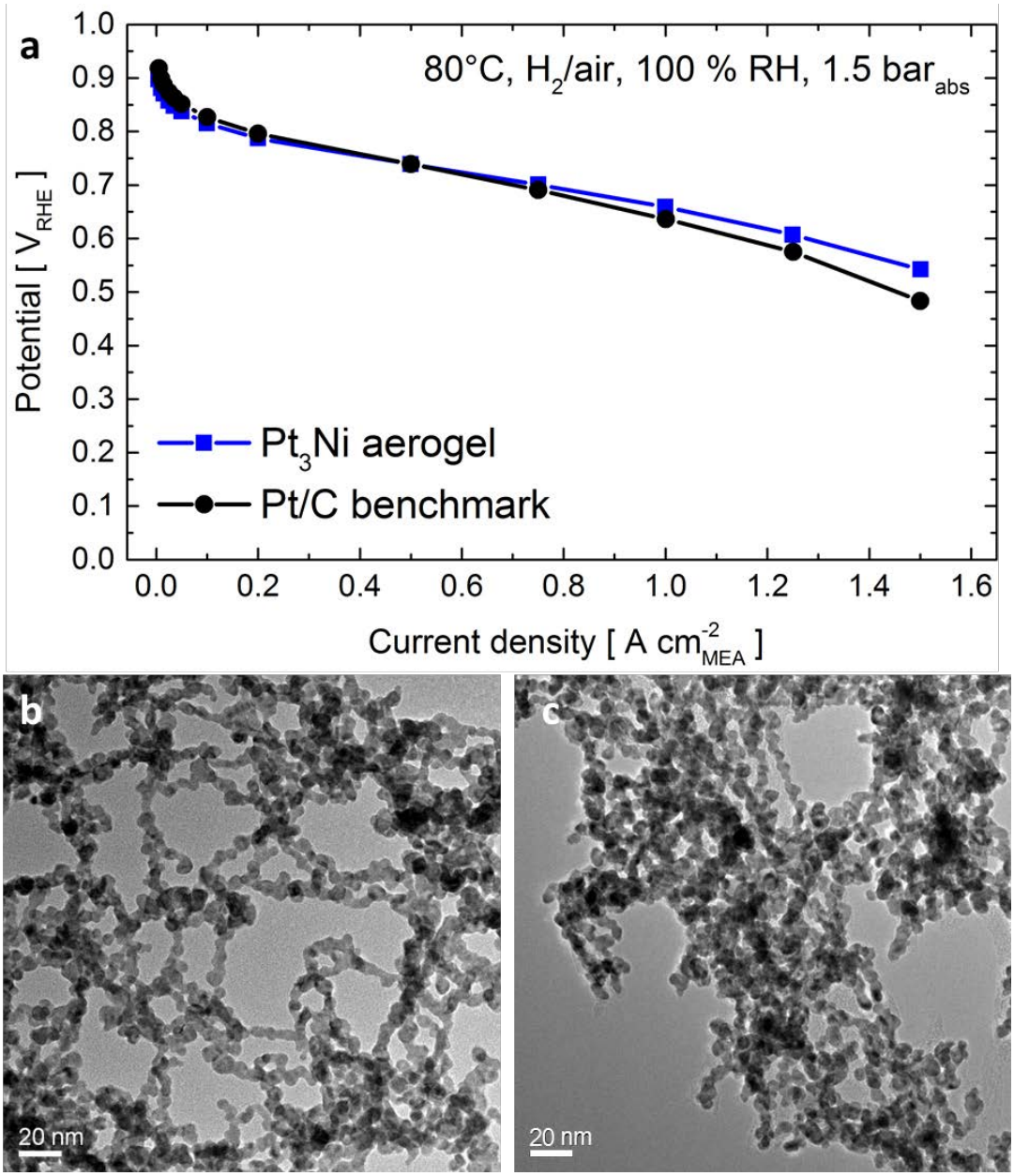

Figure 9. a) H_2/air I/E curves for Pt_3Ni aerogel and Pt/C benchmark MEAs with comparable cathode loadings of ≈ 0.3 mg_{Pt}/cm^2_{MEA}. TEM images of Pt_3Ni aerogel b) before and c) after processing into an ink for the preparation of the CL.

Author biographies and photographs

Thomas J. Schmidt studied chemistry at the University of Ulm, Gemany and then continued his career as postdoc and scientist at Lawrence Berkeley National Laboratory and at Paul Scherrer Institute (PSI). After eight years in industrial fuel cell research (BASF Fuel Cell) as Director of R&D, he became Chair of Electrochemistry at ETH Zürich and Head of the Electrochemistry Laboratory at PSI in 2011. Since 2014, he also acts a Director of the Swiss Competence Center for Energy Research (SCCER) Heat & Electricity Storage. His work is focused on all aspects of electrochemical energy conversion and storage.

Alexander Eychmüller started his academic career in Göttingen with studies of physics (Ph.D., MPI for Biophysical Chemistry, Prof. A. Weller and Dr. K. H. Grellmann) and continued at UCLA (postdoc with Prof. M. A. El-Sayed), Berlin (HMI with Prof. A. Henglein), and the University of Hamburg (with Prof. H. Weller). Since 2005 he holds the chair in Physical Chemistry at TU Dresden. His research interests include the synthesis and characterization of nanosized objects and their photophysical, electrochemical, and structural properties.

Table of contents

Unsupported electrocatalysts derived from tailored noble metal nanostructures emerged as a promising catalyst candidate for fuel cells due to the elimination of support corrosion. Recent advances in the design, synthesis and characterization of carbon-free electrocatalysts are summarized. Their electrocatalytic performances for oxygen reduction are compared and discussed, and examples of successful catalyst transfer to polymer electrolyte fuel cells are highlighted.

Keyword: unsupported electrocatalyst, metallic aerogel, oxygen reduction reaction, fuel cell, nanomaterial

Bin Cai, Sebastian Henning, Juan Herranz, Thomas J. Schmidt* and Alexander Eychmüller*

Nanostructuring noble metals as unsupported electrocatalysts for polymer electrolyte fuel cells